

## Advances in Flexible Perovskite Solar Cells: A Comprehensive Review

Sikandar Aftab, Sajjad Hussain, Fahmid Kabir,  
Muhammad Aslam, Altaf Hussain Rajpar,  
Abdullah G. Al-Sehemi



PII: S2211-2855(23)00949-7

DOI: <https://doi.org/10.1016/j.nanoen.2023.109112>

Reference: NANOEN109112

To appear in: *Nano Energy*

Received date: 15 September 2023

Revised date: 11 November 2023

Accepted date: 19 November 2023

Please cite this article as: Sikandar Aftab, Sajjad Hussain, Fahmid Kabir, Muhammad Aslam, Altaf Hussain Rajpar and Abdullah G. Al-Sehemi, Advances in Flexible Perovskite Solar Cells: A Comprehensive Review, *Nano Energy*, (2023) doi:<https://doi.org/10.1016/j.nanoen.2023.109112>

This is a PDF file of an article that has undergone enhancements after acceptance, such as the addition of a cover page and metadata, and formatting for readability, but it is not yet the definitive version of record. This version will undergo additional copyediting, typesetting and review before it is published in its final form, but we are providing this version to give early visibility of the article. Please note that, during the production process, errors may be discovered which could affect the content, and all legal disclaimers that apply to the journal pertain.

© 2023 Published by Elsevier.

# Advances in Flexible Perovskite Solar Cells: A Comprehensive Review

Sikandar Aftab<sup>1</sup>, Sajjad Hussain<sup>2</sup>, Fahmid Kabir<sup>3</sup>, Muhammad Aslam<sup>4</sup>, Altaf Hussain Rajpar<sup>5</sup>,  
and Abdullah G. Al-Sehemi<sup>6</sup>

<sup>1</sup> Department of Intelligent Mechatronics Engineering, Sejong University, Seoul 05006, South Korea

<sup>2</sup> Department of Nanotechnology and Advanced Materials Engineering, Sejong University, Seoul, South Korea

<sup>3</sup> School of Engineering Science, Simon Fraser University, Burnaby, British Columbia V5A 1S6, Canada

<sup>4</sup> Institute of Physics and Technology, Ural Federal University, Mira Str.19, 620002 Yekaterinburg, Russia

<sup>5</sup> Department of Mechanical Engineering, College of Engineering, Jouf University, 72388 Sakaka, Saudi Arabia

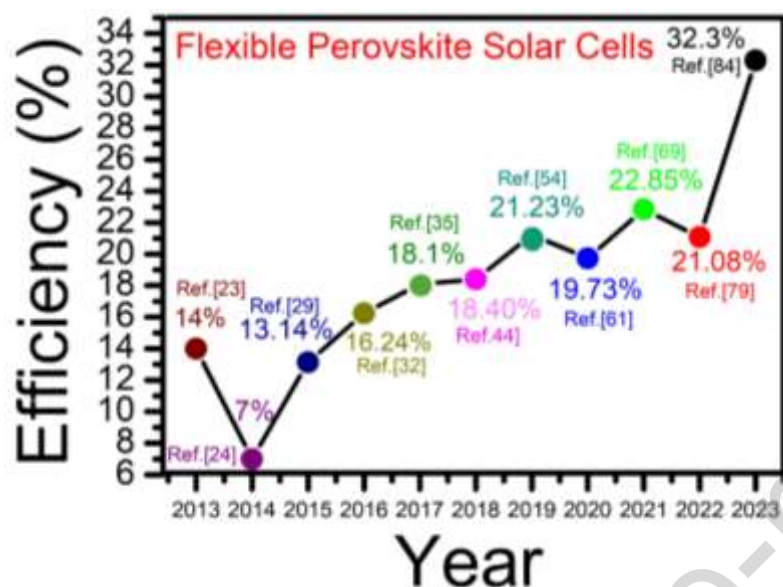
<sup>6</sup> Research Center for Advanced Materials Science (RCAMS), King Khalid University, Abha, 61413, Saudi Arabia

<sup>7</sup> Department of Chemistry, College of Science, King Khalid University, Abha, 61413, Saudi Arabia

\*Email# aftab@sejong.ac.kr

**Abstract:** Flexible perovskite solar cells (F-PSCs) have received much attention because of their exceptional potential in combining the high efficiency of perovskite materials with the adaptability of flexible substrates. This review sheds light on the dynamic and multifaceted landscape of F-PSC research, highlighting a range of cutting-edge configurations and strategies. Together, these strategies perfectly capture the unwavering dedication to improving PSC's flexibility, stability, and cost-effectiveness—a crucial pursuit in hastening their seamless integration into the main energy grid. The review outlines significant developments in various facets of F-PSC technology within this context. These encompass groundbreaking developments derived from various reports, such as optimizing tuning efficiency in F-PSCs, enhancing performance achieved through interfacial engineering in F-PSCs, and assessing stability in F-PSCs in terms of both environmental and mechanical factors. These many different lines of inquiry highlight the researchers' unwavering commitment to the constant development of F-PSCs. These technological advancements have the potential to reshape the renewable energy landscape as they continue to develop and mature, bringing us one step closer to the widespread adoption and use of sustainable and adaptable solar solutions. This in-depth analysis gives readers a tantalizing glimpse into the fascinating trends pushing F-PSCs to the fore of clean energy innovation.

## Graphical abstract



**Keywords:** flexible perovskite solar cells, 2D/3D materials, carbon-based materials, grain boundaries, dual-interface reinforcement

## 1. Introduction

Renewable energy technology has seen a revolutionary and promising development with the development of flexible perovskite solar cells (F-PSCs).[1-7] These solar cells provide a remarkable blend of high efficiency, low cost, and unmatched flexibility by utilizing the unique qualities of perovskite materials.[5] They open new horizons for integrating various applications, including wearable electronics, portable devices, curved surfaces, and irregular structures.[8-10] Traditional silicon-based solar cells are inflexible and difficult to install. A class of materials with a distinctive crystal structure motivated by the natural mineral perovskite is referred to as "perovskite." [1-5, 11-15] PSCs are created to effectively use the photovoltaic (PV) effect to convert sunlight into electricity by typically consisting of a thin layer of these substances sandwiched between conductive electrodes.[1-5] This distinctive design enables the creation of

thin, flexible, and even transparent solar panels, enabling cutting-edge designs and unmatched versatility in energy production. The remarkable power conversion efficiency (PCE) of F-PSCs is one of their most alluring characteristics. These PSCs' efficiency has significantly improved over the past few years, rivalling the performance of conventional silicon-based technologies thanks to intensive research and development efforts.[1-5, 11-14, 16] Additionally, the production of PSCs is relatively less complicated and resource-intensive, which could result in lower production costs and a more sustainable energy future.[17]

The ability of F-PSCs to resist damage brought on by mechanical external stress is crucial. Even though it has been claimed that a F-PSC has excellent mechanical properties for cyclic bending, research has shown that it is more resistant to convex bending (bend-in) than concave bending (bend-out).[18] The flexible mini-module device, measuring 7 cm by 7 cm, performed at 16.19% and offers a fresh method for the electron transport layer (ETL) of flexible, high-efficiency PSCs.[19] This is one of the highest values for F-PSCs that have been reported, and the SnO<sub>2</sub>–TiO<sub>2</sub> hybrid solution, in particular, was very helpful in creating a consistent ETL over a sizable area. Additionally, another report investigated how much the light incident angle affects the performance of two-terminal (2T) all perovskite flexible tandem solar cells (F-TSCs). The device's total photocurrent ( $J_{ph}$ ) value is  $37.63 \text{ mA cm}^{-2}$  ( $J_{top} = 18.82 \text{ mA cm}^{-2}$ ,  $J_{bottom} = 18.81 \text{ mA cm}^{-2}$ ), and the Shockley diode equation was used to determine the theoretical PCE of 34.83%.[20] F-PSCs are the best candidates to supplement conventional silicon SCs in portable power applications.[21] The F-PSCs show promising improvements in efficiency with cross-linking, the perovskite grain boundaries act as "ligaments," and record values of 23.84% and 21.66% are obtained for devices with a surface area of 0.062 and 1.004 cm<sup>2</sup>, respectively.[21] The flexible devices also have enhanced stabilities, as evidenced by their ability to withstand over 20,000

bending cycles ( $T_{90} > 20,000$ ), maintain operational stability for more than 1,248 hours ( $T_{90} > 1,248$ ), and exhibit ambient stability in conditions of 30% relative humidity (RH) for over 3,000 hours ( $T_{90} > 3,000$ )[21]

The presence of defects at the interfaces between perovskite and charge transport layers leads to a notable decrease in the efficiency and stability of F-PSCs due to charge non-radiative recombination loss.[22] To enhance transportation speed and optimize carrier collection, implementing a dual-interface engineering technique proves beneficial in reducing interface defect density and mitigating unfavourable non-radiative recombination loss to a great extent. The optimized rigid and F-PSCs exhibit exceptional mechanical reliability, resulting in significantly higher PCE of 20.06% and 23.11% compared to the pristine devices. Furthermore, these PSCs lost ~9% of their initial PCE after undergoing 5000 bending cycles with a 10 mm bending radius.[22] A dual low-temperature (100 °C) approach is also used to demonstrate highly efficient devices on PET, with efficiencies of 28.9%, allowing for seamless integration with wearable and portable Internet of Things electronic devices and smart building and extending the range of indoor applications.

In this review article, we concentrated on F-PSCs in a variety of facets, and These include ground-breaking major aspects grouped from several reports, like tuning efficiency of F-PSCs, enhanced performance through interfacial engineering in F-PSCs, and stability in F-PSCs such as environmental and mechanical. These arrangements each represent a distinct line of inquiry for advancing F-PSCs. The transformational potential of F-PSCs becomes more palpable as we delve deeper into these many-faceted areas of investigation, providing a promising road to adopting renewable energy on a broad and sustainable scale. **Figure 1** displays the overview and the annualized efficiencies of F-PSCs.

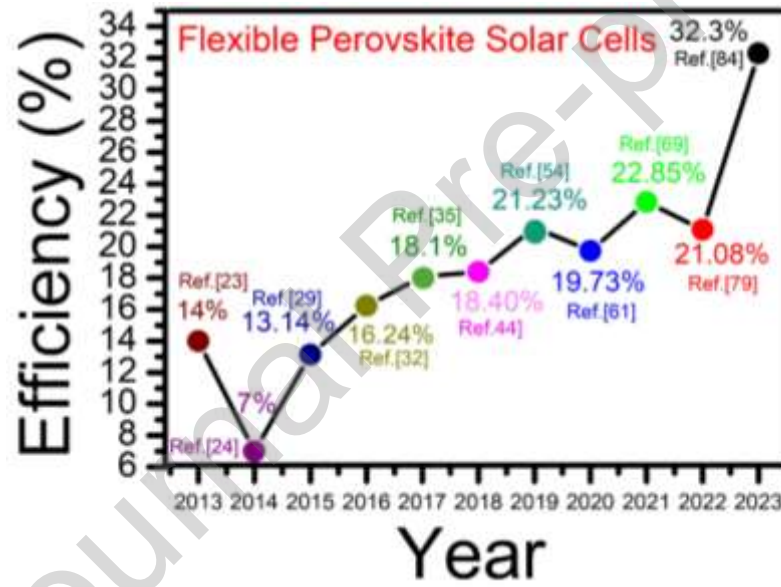


**Figure 1.** An overview of F-PSCs' yearly performance assessments, related references, and different PV metrics are shown in Table 1.

**Table 1:** A comparison of various F-PSCs on different substrates.

Structure of PSC	V <sub>oc</sub> (V)	J <sub>sc</sub> (mA/cm <sup>2</sup> )	FF	PCE	Year	Ref
PET/Ag-mesh/PH1000/PEDOT:PSS/Perovskite/PCBM/Al (active area= 0.08 cm <sup>2</sup> )	0.91	19.5	0.800	14.0	2013	[23]
PET/AZO/Ag/AZO/PEDOT:PSS/PolyTPD/MAPbI <sub>3</sub> /PCBM/Au (active area= 0.12 cm <sup>2</sup> )	1.05	16.1	0.67	7	2014	[24]
Ti foil/TiO <sub>2</sub> BL/MP-TiO <sub>2</sub> /MAPbI <sub>3</sub> /Spiro/Ag (8 nm) (active area= 0.135 cm <sup>2</sup> )	0.766 ± 0.064	2.97 ± 1.28	0.21 ± 0.04	0.46 ± 0.18	2015	[25]
Ti foil/TiO <sub>2</sub> BL/MP-TiO <sub>2</sub> /MAPbI <sub>3</sub> /Spiro/Ag (12 nm) (active area= 0.135 cm <sup>2</sup> )	0.855 ± 0.023	7.04 ± 1.74	0.68 ± 0.05	4.07 ± 1.08	2015	[25]
Ti foil/TiO <sub>2</sub> BL/MP-TiO <sub>2</sub> /MAPbI <sub>3</sub> /Spiro/Ag (16 nm) (active area= 0.135 cm <sup>2</sup> )	0.835 ± 0.045	5.45 ± 1.00	0.59 ± 0.05	2.70 ± 0.66	2015	[25]

Ti foil/TiO <sub>2</sub> BL/MP-TiO <sub>2</sub> /MAPbI <sub>3</sub> /Spiro/Ag (20 nm) (active area= 0.135 cm <sup>2</sup> )	0.756 ± 0.061	4.53 ± 0.94	0.58 ± 0.08	2.03 ± 0.65	2015	[25]
Ti foil/TiO <sub>2</sub> NTs+MAPbI <sub>3</sub> /CNTs+Spiro (125 μm Ti) (active area= 0.16 cm <sup>2</sup> )	0.66 ± 0.02	10.33 ± 1.36	0.57 ± 0.03	3.90 ± 0.50	2015	[26]
Ti foil/TiO <sub>2</sub> NTs+MAPbI <sub>3</sub> /CNTs+Spiro (125 μm Ti-TiCl <sub>4</sub> treated) (active area= 0.16 cm <sup>2</sup> )	0.77 ± 0.01	12.24 ± 0.73	0.60 ± 0.01	5.73 ± 0.28	2015	[26]
Ti foil/TiO <sub>2</sub> NTs+MAPbI <sub>3</sub> /CNTs+Spiro (25 μm Ti) (active area= 0.16 cm <sup>2</sup> )	0.80 ± 0.01	11.60 ± 1.34	0.52 ± 0.06	4.83 ± 0.74	2015	[26]
Ti foil/TiO <sub>2</sub> NTs+MAPbI <sub>3</sub> /CNTs+Spiro (25 μm Ti-TiCl <sub>4</sub> treated) (active area= 0.16 cm <sup>2</sup> )	0.97 ± 0.02	12.61 ± 1.25	0.60 ± 0.07	7.38 ± 0.73	2015	[26]
Ti/TiO <sub>2</sub> BL/TiO <sub>2</sub> +MAPbI <sub>3</sub> /Spiro/ITO (active area= 0.135 cm <sup>2</sup> )	0.958 ± 0.036	15.54 ± 0.68	0.54 ± 0.01	8.02 ± 0.70	2015	[27]
Ti/TiO <sub>2</sub> BL/TiO <sub>2</sub> +MAPbI <sub>3</sub> /Spiro/Ag 1 nm_ITO (active area= 0.135 cm <sup>2</sup> )	0.960 ± 0.039	17.37 ± 0.68	0.59 ± 0.02	9.78 ± 0.91	2015	[27]
Ti/TiO <sub>2</sub> BL/TiO <sub>2</sub> +MAPbI <sub>3</sub> /Spiro/Ag 2 nm_ITO (active area= 0.135 cm <sup>2</sup> )	0.964 ± 0.032	16.01 ± 0.57	0.62 ± 0.01	9.65 ± 0.57	2015	[27]
Ti/TiO <sub>2</sub> BL/TiO <sub>2</sub> +MAPbI <sub>3</sub> /Spiro/Ag 3 nm_ITO (active area= 0.135 cm <sup>2</sup> )	0.962 ± 0.032	13.95 ± 0.49	0.65 ± 0.01	8.67 ± 0.60	2015	[27]
PET/ITO/PEDOT:PSS(VPAI4083)/ MAPbI <sub>3</sub> /PCBM/TiO <sub>2</sub> /Al (HTM deposition=Spin) (active area= 0.16 cm <sup>2</sup> )	0.839	11.2	0.455	4.3	2015	[28]
PET/ITO/PEDOT:PSS(VPAI4083)/ MAPbI <sub>3</sub> /PCBM/TiO <sub>2</sub> /Al (HTM deposition=Spray) (active area= 0.16 cm <sup>2</sup> )	0.736	7.2	0.45	2.3	2015	[28]
PET/PEDOT:PSS(m-PH1000)+EG/PEDOT:PSS(VPAI4083)/ MAPbI <sub>3</sub> /PCBM/TiO <sub>2</sub> /Al (HTM deposition=Spin) (active area= 0.16 cm <sup>2</sup> )	0.269	4	0.25	0.3	2015	[28]
PET/PEDOT:PSS(m-PH1000)+EG/PEDOT:PSS(VPAI4083)/ MAPbI <sub>3</sub> /PCBM/TiO <sub>2</sub> /Al (HTM deposition=Spray) (active area= 0.16 cm <sup>2</sup> )	0.849	11	0.44	4.2	2015	[28]
PET/PEDOT:PSS(pristine-PH1000)+EG/PEDOT:PSS(VPAI4083)/ MAPbI <sub>3</sub> /PCBM/TiO <sub>2</sub> /Al (HTM deposition=Spray) (active area= 0.16 cm <sup>2</sup> )	0.853	6.6	0.36	2.0	2015	[28]
Willow galss/ITO/ZnO/Perovskite/Spiro-OMeTAD/Au (without nanocone AR) (active area= 0.04 cm <sup>2</sup> )	0.97	17.7	0.70	12.06	2015	[29]
<b>Willow galss/ITO/ZnO/Perovskite/Spiro-OMeTAD/Au (with nanocone AR) (active area= 0.04 cm<sup>2</sup>)</b>	<b>0.98</b>	<b>19.3</b>	<b>0.69</b>	<b>13.14</b>	<b>2015</b>	<b>[29]</b>
PET/AgNWs/PEDOT:PSS/Perovskite/PCBM/Al (active area= 1.2 cm <sup>2</sup> )	0.92	21.1	0.670	11.2	2015	[30]
PET/HNO <sub>3</sub> -SWNT/PEDOT:PSS/Perovskite/PC61BM/Al (active area= 3 x 3 mm <sup>2</sup> )	0.77	14.4	0.550	6.1	2015	[31]
PET/Graphene/P3HT/MAPbI <sub>3</sub> /PCBM/Ag (P3HT concentration: 5.0 mg/ml; P3HT Thickness: 17 nm) (active area= 4 mm <sup>2</sup> )	1.03	18.39	75.0	14.20	2016	[32]
PET/Graphene/P3HT/MAPbI <sub>3</sub> /PCBM/Ag (P3HT concentration: 2.5 mg/ml; P3HT Thickness: 8 nm) (active area= 4 mm <sup>2</sup> )	1.01	19.74	73.4	14.64	2016	[32]
PET/Graphene/P3HT/MAPbI <sub>3</sub> /PCBM/Ag (P3HT concentration: 1.25 mg/ml; P3HT Thickness: 4 nm) (active area= 4 mm <sup>2</sup> )	0.97	17.76	69.5	11.97	2016	[32]
PET/Graphene/P3HT/MAPbI <sub>3</sub> /PCBM/Ag (MAI:PbI <sub>2</sub> :DMSO= 1:1:3) (active area= 4 mm <sup>2</sup> )	0.97	18.83	74.9	13.68	2016	[32]
<b>PET/Graphene/P3HT/MAPbI<sub>3</sub>/PCBM/Ag (MAI:PbI<sub>2</sub>:DMSO= 1:1:2) (active area= 4 mm<sup>2</sup>)</b>	<b>1.02</b>	<b>21.33</b>	<b>74.6</b>	<b>16.24</b>	<b>2016</b>	<b>[32]</b>
PET/Graphene/P3HT/MAPbI <sub>3</sub> /PCBM/Ag (MAI:PbI <sub>2</sub> :DMSO= 1:1:1) (active area= 4 mm <sup>2</sup> )	1.00	20.60	60.3	12.42	2016	[32]
PET/Graphene/P3HT/MAPbI <sub>3</sub> /PCBM/Ag (without coating ZEOCOAT™ layers) (active area= 4 mm <sup>2</sup> )	0.96	18.17	59.5	10.38	2016	[32]
PET/Graphene/P3HT/MAPbI <sub>3</sub> /PCBM/Ag (with coating ZEOCOAT™ layers) (active area= 4 mm <sup>2</sup> )	1.04	18.58	59.4	11.48	2016	[32]
PEN/ITO/CuCrO/Perovskite/PCBM/BCP/Ag (active area= 0.10 cm <sup>2</sup> )	1.07	21.1	0.690	15.6	2017	[33]
PET/ITO/PTAA/FAMAPbI <sub>3</sub> -Br <sub>2</sub> /C60/BCP/Cu (active area= 10 mm <sup>2</sup> )	1.06	22.80	0.746	18.10	2017	[34]
MgF <sub>2</sub> /Willow glass/ITO/SnO <sub>2</sub> /FAMACs/Spiro/MoO <sub>3</sub> /Al (active area= 0.10 cm <sup>2</sup> )	1.078	22.97	0.698	17.3	2017	[35]
MgF <sub>2</sub> /Willow glass/AZO/SnO <sub>2</sub> /FAMACs/Spiro/MoO <sub>3</sub> /Al (active area= 0.10 cm <sup>2</sup> )	0.999	21.99	0.557	12.2	2017	[35]
<b>MgF<sub>2</sub>/Willow glass/IZO/SnO<sub>2</sub>/FAMACs/Spiro/MoO<sub>3</sub>/Al (active area= 0.10 cm<sup>2</sup>)</b>	<b>1.064</b>	<b>22.16</b>	<b>0.752</b>	<b>18.1</b>	<b>2017</b>	<b>[35]</b>
PET/APTES/ AuCl <sub>3</sub> -GR/ PEDOT:PSS/ PCBM/FAPbI <sub>3-x</sub> Br <sub>x</sub> /PCBM/Al (active area= 0.16 cm <sup>2</sup> )	1.08	21.2	0.781	17.9	2017	[36]
PET/APTES/ AuCl <sub>3</sub> -GR/ PEDOT:PSS/MAPbI <sub>3</sub> /PCBM/Al (active area= 0.16 cm <sup>2</sup> )	1.10	18.8	0.779	16.1	2017	[36]
PET/AuCl <sub>3</sub> -GR/ PEDOT:PSS/MAPbI <sub>3</sub> /PCBM/Al (active area= 0.16 cm <sup>2</sup> )	1.10	18.7	0.78	16	2017	[36]
PET/ITO/ PEDOT:PSS/MAPbI <sub>3</sub> /PCBM/ Al (active area= 0.16 cm <sup>2</sup> )	1.10	18.2	0.791	15.8	2017	[36]
Au/Spiro/MAPbI <sub>3</sub> /ZnO/c-AZO/AgNW/AZO/PES (active area= 0.06 cm <sup>2</sup> )	0.93 ± 0.08	14.3 ± 2.8	0.558 ± 0.091	7.53 ± 2.23	2017	[37]
Au/Spiro/MAPbI <sub>3</sub> /ZnO/AZO/AgNW/AZO/PES (active area= 0.06 cm <sup>2</sup> )	0.56 ± 0.25	0.03 ± 0.02	0.252 ± 0.008	0.004	2017	[37]
Au/Spiro/MAPbI <sub>3</sub> /ZnO/a-AZO/AgNW/AZO/ PES (active area= 0.06 cm <sup>2</sup> )	1.04 ± 0.02	18.0 ± 1.0	0.627 ± 0.059	11.77 ± 1.64	2017	[37]
PEN/Graphene/MoO <sub>3</sub> /PEDOT:PSS/MAPbI <sub>3</sub> /C60/BCP/LiF/Al (active area= 1.77 mm <sup>2</sup> )	0.99 ± 0.02	21.0 ± 0.5	0.72 ± 0.03	15.0 ± 1.0	2017	[38]
PEN/ITO/MoO <sub>3</sub> /PEDOT:PSS/MAPbI <sub>3</sub> /C60/BCP/LiF/Al (active area= 1.77 mm <sup>2</sup> )	0.97 ± 0.01	20.8 ± 0.5	0.81 ± 0.02	16.4 ± 0.5	2017	[38]
Paper/Au/SnO <sub>2</sub> /meso-TiO <sub>2</sub> /CH <sub>3</sub> NH <sub>3</sub> PbI <sub>3</sub> /Spiro-OMeTAD/ MoO <sub>3</sub> /Au (active area= 0.10 cm <sup>2</sup> )	0.61	8.9	0.508	2.7	2017	[39]
PET/ITO/SnO <sub>2</sub> /meso-TiO <sub>2</sub> /CH <sub>3</sub> NH <sub>3</sub> PbI <sub>3</sub> /Spiro-OMeTAD/ MoO <sub>3</sub> /Au (active area= 0.10 cm <sup>2</sup> )	1.07	14.9	0.572	9.1	2017	[39]
Au/PTAA/MAPbI <sub>3</sub> /ZnO/ITO/PET (active area= 0.16 cm <sup>2</sup> )	1.1	17.4	77.5	14.8	2017	[40]
Au/PTAA/MAPbI <sub>3</sub> /ZnO/ITO/CPI (active area= 0.16 cm <sup>2</sup> )	1.1	17.6	79.4	15.5	2017	[40]
NOA63/Au/PEDOT:PSS/Perovskite/PCBM/MoO <sub>3</sub> /Au/Ag/MoO <sub>3</sub> /Alq <sub>3</sub>	0.94	14.6	0.623	8.6	2017	[41]
SU-8/MoO <sub>3</sub> /Au/PEDOT:PSS/Perovskite/PCBM/Ca/Ag (active area= 4 mm <sup>2</sup> )	0.93	13.2	0.739	9.1	2017	[42]
PET/PEDOT:PSS/Perovskite/PTCDI/Cr/Au (active area= 0.14-0.15 cm <sup>2</sup> )	0.92	17.6	0.730	11.9	2017	[43]
MgF <sub>2</sub> /PET/ITO/Nb <sub>2</sub> O <sub>5</sub> /MAPbI <sub>3</sub> /Spiro-OMeTAD/Au (active area= 0.052 cm <sup>2</sup> )	1.090	21.97	0.711	17.03	2018	[44]
<b>MgF<sub>2</sub>/PET/ITO/Nb<sub>2</sub>O<sub>5</sub>/MAPbI<sub>3</sub> -dimethyl sulfide/Spiro-OMeTAD/Au (Flat) (active area= 0.052 cm<sup>2</sup>)</b>	<b>1.103</b>	<b>22.48</b>	<b>0.742</b>	<b>18.40</b>	<b>2018</b>	<b>[44]</b>
MgF <sub>2</sub> /PET/ITO/Nb <sub>2</sub> O <sub>5</sub> /MAPbI <sub>3</sub> -dimethyl sulfide/Spiro-OMeTAD/Au (R <sub>14</sub> - bending) (active area= 0.052 cm <sup>2</sup> )	1.101	22.36	0.739	18.19	2018	[44]
MgF <sub>2</sub> /PET/ITO/Nb <sub>2</sub> O <sub>5</sub> /MAPbI <sub>3</sub> -dimethyl sulfide/Spiro-OMeTAD/Au (R <sub>10</sub> - bending) (active area= 0.052 cm <sup>2</sup> )	1.102	21.97	0.716	17.34	2018	[44]
MgF <sub>2</sub> /PET/ITO/Nb <sub>2</sub> O <sub>5</sub> /MAPbI <sub>3</sub> -dimethyl sulfide/Spiro-OMeTAD/Au (R <sub>6</sub> - bending) (active area= 0.052 cm <sup>2</sup> )	1.082	21.76	0.679	15.98	2018	[44]
MgF <sub>2</sub> /PET/ITO/Nb <sub>2</sub> O <sub>5</sub> /MAPbI <sub>3</sub> -dimethyl sulfide/Spiro-OMeTAD/Au (R <sub>5</sub> - bending) (active area= 0.052 cm <sup>2</sup> )	1.069	21.72	0.682	15.84	2018	[44]
MgF <sub>2</sub> /PET/ITO/Nb <sub>2</sub> O <sub>5</sub> /MAPbI <sub>3</sub> -dimethyl sulfide/Spiro-OMeTAD/Au (R <sub>4</sub> - bending) (active area= 0.052 cm <sup>2</sup> )	1.076	21.43	0.659	15.20	2018	[44]
PEN/ITO/Cu:NiO/MAPbI <sub>3</sub> /C60/BCP/Ag (active area= 0.08 cm <sup>2</sup> )	1.10	21.45	0.738	17.41	2018	[45]
PEN/ITO/NiO/MAPbI <sub>3</sub> /C60/BCP/Ag (active area= 0.08 cm <sup>2</sup> ) (active area= 0.14 cm <sup>2</sup> )	1.10	21.73	0.753	18.02	2018	[45]
Glass/ITO/SnO <sub>2</sub> -EDTA/CsFAPbI <sub>3</sub> /Spiro-OMeTAD/Au (E-SnO <sub>2</sub> R <sub>0</sub> ) (active area= 0.1134 cm <sup>2</sup> )	1.09	23.42	0.716	18.28	2018	[46]
Glass/ITO/SnO <sub>2</sub> -EDTA/CsFAPbI <sub>3</sub> /Spiro-OMeTAD/Au (E-SnO <sub>2</sub> R <sub>14</sub> -500) (active area= 0.1134 cm <sup>2</sup> )	1.09	23.42	0.715	18.25	2018	[46]
Glass/ITO/SnO <sub>2</sub> -EDTA/CsFAPbI <sub>3</sub> /Spiro-OMeTAD/Au (E-SnO <sub>2</sub> R <sub>12</sub> -500) (active area= 0.1134 cm <sup>2</sup> )	1.08	23.11	0.714	17.82	2018	[46]
Glass/ITO/SnO <sub>2</sub> -EDTA/CsFAPbI <sub>3</sub> /Spiro-OMeTAD/Au (E-SnO <sub>2</sub> R <sub>7</sub> -500) (active area= 0.1134 cm <sup>2</sup> )	1.08	22.66	0.688	16.84	2018	[46]
Ti/TiO <sub>2</sub> / CH <sub>3</sub> NH <sub>3</sub> PbI <sub>3</sub> /HTM/CH <sub>3</sub> NH <sub>3</sub> PbI <sub>3</sub> /Cu/Au (Oxide layer thickness= ~25 nm) (active area= 0.14 cm <sup>2</sup> )	0.659	15.6	0.41	4.24	2018	[47]
Ti/TiO <sub>2</sub> / CH <sub>3</sub> NH <sub>3</sub> PbI <sub>3</sub> /HTM/CH <sub>3</sub> NH <sub>3</sub> PbI <sub>3</sub> /Cu/Au (Oxide layer thickness= ~50 nm) (active area= 0.14 cm <sup>2</sup> )	0.910	16.2	0.58	8.56	2018	[47]
Ti/TiO <sub>2</sub> / CH <sub>3</sub> NH <sub>3</sub> PbI <sub>3</sub> /HTM/CH <sub>3</sub> NH <sub>3</sub> PbI <sub>3</sub> /Cu/Au (Oxide layer thickness= ~80 nm) (active area= 0.14 cm <sup>2</sup> )	0.878	9.45	0.52	4.45	2018	[47]
Ti/TiO <sub>2</sub> / CH <sub>3</sub> NH <sub>3</sub> PbI <sub>3</sub> /HTM/CH <sub>3</sub> NH <sub>3</sub> PbI <sub>3</sub> /Cu/Au (Annealing temperature= 500°C ) (active area= 0.14 cm <sup>2</sup> )	0.95	17.1	0.60	9.70	2018	[47]

Ti/TiO <sub>2</sub> /CH <sub>3</sub> NH <sub>3</sub> PbI <sub>3</sub> /HTM/CH <sub>3</sub> NH <sub>3</sub> PbI <sub>3</sub> /Cu/Au (Annealing temperature= 600°C) (active area= 0.14 cm <sup>2</sup> )	0.94	14.2	0.49	6.58	2018	[47]
Ti/TiO <sub>2</sub> /CH <sub>3</sub> NH <sub>3</sub> PbI <sub>3</sub> /HTM/CH <sub>3</sub> NH <sub>3</sub> PbI <sub>3</sub> /Cu/Au (Annealing temperature= 700°C) (active area= 0.14 cm <sup>2</sup> )	0.89	13.1	0.48	6.11	2018	[47]
Ti/TiO <sub>2</sub> /CH <sub>3</sub> NH <sub>3</sub> PbI <sub>3</sub> /HTM/CH <sub>3</sub> NH <sub>3</sub> PbI <sub>3</sub> /Cu/Au (Annealing temperature= 400°C for 15 minute) (active area= 0.14 cm <sup>2</sup> )	1.02	17.2	0.68	11.9	2018	[47]
Ti/TiO <sub>2</sub> /CH <sub>3</sub> NH <sub>3</sub> PbI <sub>3</sub> /HTM/CH <sub>3</sub> NH <sub>3</sub> PbI <sub>3</sub> /Cu/Au (Annealing temperature= 400°C for 30 minute) (active area= 0.14 cm <sup>2</sup> )	1.03	17.7	0.71	13.0	2018	[47]
Ti/TiO <sub>2</sub> /CH <sub>3</sub> NH <sub>3</sub> PbI <sub>3</sub> /HTM/CH <sub>3</sub> NH <sub>3</sub> PbI <sub>3</sub> /Cu/Au (Annealing temperature= 400°C for 60 minute) (active area= 0.14 cm <sup>2</sup> )	1.09	17.9	0.74	14.7	2018	[47]
Ti/TiO <sub>2</sub> /CH <sub>3</sub> NH <sub>3</sub> PbI <sub>3</sub> /HTM/CH <sub>3</sub> NH <sub>3</sub> PbI <sub>3</sub> /Cu/Au (Annealing temperature= 400°C for 120 minute) (active area= 0.14 cm <sup>2</sup> )	1.07	17.8	0.73	14.0	2018	[47]
Ti/TiO <sub>2</sub> /Perovskite/PTAA/Graphene/PDMS (Number of graphene layer= 1) (active area= 1 cm <sup>2</sup> )	1.06	19.4	0.679	14.0	2018	[48]
Ti/TiO <sub>2</sub> /Perovskite/PTAA/Graphene/PDMS (Number of graphene layer= 2) (active area= 1 cm <sup>2</sup> )	1.06	19.0	0.715	14.4	2018	[48]
Ti/TiO <sub>2</sub> /Perovskite/PTAA/Graphene/PDMS (Number of graphene layer= 3) (active area= 1 cm <sup>2</sup> )	1.08	18.7	0.744	15.0	2018	[48]
Ti/TiO <sub>2</sub> /Perovskite/PTAA/Graphene/PDMS (Number of graphene layer= 4) (active area= 1 cm <sup>2</sup> )	1.08	18.4	0.738	14.7	2018	[48]
PET/ITO/SnO <sub>2</sub> -KOH/Perovskite/Spiro-OMeTAD/Au (active area= 0.16 cm <sup>2</sup> )	1.00	22.3	0.700	15.6	2018	[49]
PEN/ITO/SnO <sub>2</sub> /Perovskite/Spiro-OMeTAD/Au (active area= 0.0405 cm <sup>2</sup> )	1.08	21.3	0.749	17.3	2019	[50]
PEN/ITO/SnO <sub>2</sub> -CPTA/Perovskite/Spiro-OMeTAD/Au (active area= 0.1 cm <sup>2</sup> )	1.08	22.4	0.750	18.3	2019	[51]
PET/ITO/TiO <sub>2</sub> /MAPbI <sub>3</sub> /Spiro-OMeTAD/Au (active area= 7.25 mm <sup>2</sup> )	1.07	20.17	0.73	15.8	2019	[52]
PET/ITO/TiO <sub>2</sub> /MAPbI <sub>3</sub> /Spiro-OMeTAD/Au ( $\Delta 1.0$ nm $\mu\text{m}^{-1}$ ) (active area= 7.25 mm <sup>2</sup> )	0.97	19.86	0.72	13.8	2019	[52]
PET/ITO/TiO <sub>2</sub> /MAPbI <sub>3</sub> -C-PCBOD/Spiro-OMeTAD/Au (active area= 7.25 mm <sup>2</sup> )	1.10	21.62	0.76	18.1	2019	[52]
PET/ITO/TiO <sub>2</sub> /MAPbI <sub>3</sub> -C-PCBOD/Spiro-OMeTAD/Au ( $\Delta 1.0$ nm $\mu\text{m}^{-1}$ ) (active area= 7.25 mm <sup>2</sup> )	1.07	21.47	0.76	17.5	2019	[52]
PET/PEDOT:PSS/MAPIB <sub>3</sub> /C <sub>60</sub> /BCP/Cu/Parylene (active area= 1.2 cm <sup>2</sup> )	0.87	20.76	0.75	13.62	2019	[53]
PEN/ITO/SnO <sub>2</sub> /FAI-PbI <sub>2</sub> -NMP+MACI/Spiro-OMeTAD/Au (0 % MACI) (active area= 0.09 cm <sup>2</sup> )	1.04	22.07	0.683	15.68	2019	[54]
PEN/ITO/SnO <sub>2</sub> /FAI-PbI <sub>2</sub> -NMP+MACI/Spiro-OMeTAD/Au (7.5 % MACI) (active area= 0.09 cm <sup>2</sup> )	1.04	23.98	0.727	18.13	2019	[54]
<b>PEN/ITO/SnO<sub>2</sub>/FAI-PbI<sub>2</sub>-NMP+MACI/Spiro-OMeTAD/Au (15 % MACI) (active area= 0.09 cm<sup>2</sup>)</b>	<b>1.08</b>	<b>24.56</b>	<b>0.800</b>	<b>21.23</b>	<b>2019</b>	<b>[54]</b>
PEN/ITO/SnO <sub>2</sub> /FAI-PbI <sub>2</sub> -NMP+MACI/Spiro-OMeTAD/Au (22.5 % MACI) (active area= 0.09 cm <sup>2</sup> )	0.98	23.84	0.739	17.28	2019	[54]
PEN/ITO/SnO <sub>2</sub> /FAI-PbI <sub>2</sub> -NMP+MACI/Spiro-OMeTAD/Au (30 % MACI) (active area= 0.09 cm <sup>2</sup> )	0.95	23.89	0.678	15.39	2019	[54]
Cellophane/OMO/CPTA/MAPIB <sub>3</sub> /Spiro-OMeTAD /Au	1.04±0.01	17.56±0.52	67.27±2.15	12.26 ±0.58	2019	[55]
b-CNF/IZO/PEDOT:PSS/Perovskite/PCBM/Ag (Curvature radius= 0 mm)	0.872	14.40	0.677	10.27	2019	[56]
b-CNF/IZO/PEDOT:PSS/Perovskite/PCBM/Ag (Curvature radius= 6 mm)	0.860	17.09	0.684	10.05	2019	[56]
b-CNF/IZO/PEDOT:PSS/Perovskite/PCBM/Ag (Curvature radius= 5 mm)	0.840	17.33	0.646	9.41	2019	[56]
b-CNF/IZO/PEDOT:PSS/Perovskite/PCBM/Ag (Curvature radius= 4 mm)	0.842	16.96	0.623	8.89	2019	[56]
b-CNF/IZO/PEDOT:PSS/Perovskite/PCBM/Ag (Curvature radius= 3 mm)	0.867	16.38	0.577	8.19	2019	[56]
b-CNF/IZO/PEDOT:PSS/Perovskite/PCBM/Ag (Curvature radius= 2 mm)	0.835	15.61	0.552	7.20	2019	[56]
PET/ITO/NiOx/Perovskite/PCBM/BCP/Ag (active area= 7 mm <sup>2</sup> )	1.05	19.2	0.679	13.6	2019	[57]
PET/ITO/m-PEDOT:PSS/Perovskite/PCBM/ PEIE/Ag (active area= 10 mm <sup>2</sup> )	0.98	21.7	0.547	11.7	2019	[58]
PET/Ni-mesh:PEDOT:PSS PH1000/MAPIB <sub>3</sub> -C-PCBOD/PCBM/BCP/Ag (active area= 7.25 mm <sup>2</sup> )	0.94	21.30	0.75	15.0	2020	[59]
PET/Ni-mesh:PEDOT:PSS PH1000/PEDOT:PSS-NiOx/MAPIB <sub>3</sub> -C-PCBOD/PCBM/BCP/Ag (PEDOT: PSS-NiOx (2:1 vol)) (active area= 7.25 mm <sup>2</sup> )	0.98	21.45	0.76	16.1	2020	[59]
PET/Ni-mesh:PEDOT:PSS PH1000/PEDOT:PSS-NiOx/MAPIB <sub>3</sub> -C-PCBOD/PCBM/BCP/Ag (PEDOT: PSS-NiOx (1:1 vol)) (active area= 7.25 mm <sup>2</sup> )	1.02	21.78	0.78	17.3	2020	[59]
PET/Ni-mesh:PEDOT:PSS PH1000/PEDOT:PSS-NiOx/MAPIB <sub>3</sub> -C-PCBOD/PCBM/BCP/Ag (PEDOT: PSS-NiOx (1:2 vol)) (active area= 7.25 mm <sup>2</sup> )	1.04	20.73	0.75	16.2	2020	[59]
MgF <sub>2</sub> / Willow glass/ITO/PTAA/MAPIB <sub>3</sub> /C <sub>60</sub> /BCP/Cu (active area= 0.052 cm <sup>2</sup> )	1.083	21.49	0.712	16.57	2020	[60]
MgF <sub>2</sub> / Willow glass/ITO/PTAA/MAPIB <sub>3</sub> -NH <sub>4</sub> Cl/C <sub>60</sub> /BCP/Cu (active area= 0.052 cm <sup>2</sup> )	1.092	22.83	0.791	19.72	2020	[60]
<b>PET/ITO/PEDOT:EVA/Perovskite/PCBM/BCP/Ag (active area= 1.01 cm<sup>2</sup>)</b>	<b>1.18±0.01</b>	<b>21.21±0.05</b>	<b>0.78±0.02</b>	<b>19.52±0.21</b>	<b>2020</b>	<b>[61]</b>
PET/ITO/PSMs /Perovskite/PCBM/BCP/Ag (active area= 1.01 cm <sup>2</sup> )	4.72±0.01	4.92±0.14	0.65±0.15	15.01±0.18	2020	[61]
PET/ITO/SnO <sub>2</sub> /Peovskite/Spiro-OMeTAD/Au (Table-top gravure-printed flexible devices: Spin-coated Spiro) (active area= 1 cm <sup>2</sup> )	1.14	22.1	0.755	19.1	2020	[62]
PET/ITO/SnO <sub>2</sub> /Peovskite/Spiro-OMeTAD/Au (Table-top gravure-printed flexible devices: Shear-coated Spiro) (active area= 1 cm <sup>2</sup> )	1.06	22.5	0.743	17.8	2020	[62]
PET/ITO/SnO <sub>2</sub> /Peovskite/Spiro-OMeTAD/Au (Table-top gravure-printed flexible devices: Gravure-printed Spiro) (active area= 1 cm <sup>2</sup> )	1.02	22.5	0.735	17.1	2020	[62]
PET/ITO/SnO <sub>2</sub> /Peovskite/Spiro-OMeTAD/Au (R2R gravure-printed flexible devices: Spin-coated Spiro) (active area= 1 cm <sup>2</sup> )	1.02	22.0	0.744	16.7	2020	[62]
PET/ITO/SnO <sub>2</sub> /Peovskite/Spiro-OMeTAD/Au (R2R gravure-printed flexible devices: Table-top Shear-coated Spiro) (active area= 1 cm <sup>2</sup> )	1.01	21.9	0.736	16.5	2020	[62]
PET/ITO/SnO <sub>2</sub> /Peovskite/Spiro-OMeTAD/Au (R2R gravure-printed flexible devices: Table-top Gravure-printed Spiro) (active area= 1 cm <sup>2</sup> )	0.99	21.9	0.721	15.6	2020	[62]
PET/ITO/SnO <sub>2</sub> /Peovskite/Spiro-OMeTAD/Au (R2R gravure-printed flexible devices: Table-top Gravure-printed P3HT) (active area= 1 cm <sup>2</sup> )	1.01	20.9	0.663	14.0	2020	[62]
PET/ITO/SnO <sub>2</sub> /Peovskite/Spiro-OMeTAD/Au (R2R gravure-printed flexible devices: R2R Gravure-printed P3HT) (active area= 1 cm <sup>2</sup> )	0.96	20.9	0.681	13.8	2020	[62]
PET/IZO/PTAA/Perovskite/PCBM/Cr/Carbon (active area= 1 cm <sup>2</sup> )	1.05	20.92	0.6897	15.18	2020	[63]
PET/IZO/PTAA/Perovskite/PCBM/Cr/Ag (active area= 1 cm <sup>2</sup> )	1.01	20.13	0.7709	15.71	2020	[63]
PET/Graphene/ZnO/PCBM/ CH <sub>3</sub> NH <sub>3</sub> PbI <sub>3</sub> /PTAA/Au (ZnO layer= 22 nm) (active area= 1.5 x 1.5 cm <sup>2</sup> )	0.72	12.32	0.63	5.6	2020	[64]
PET/Graphene/ZnO/PCBM/ CH <sub>3</sub> NH <sub>3</sub> PbI <sub>3</sub> /PTAA/Au (ZnO layer= 32 nm) (active area= 1.5 x 1.5 cm <sup>2</sup> )	0.94	18.7	0.71	12.49	2020	[64]
PET/Graphene/ZnO/PCBM/ CH <sub>3</sub> NH <sub>3</sub> PbI <sub>3</sub> /PTAA/Au (ZnO layer= 42 nm) (active area= 1.5 x 1.5 cm <sup>2</sup> )	0.84	15.64	0.65	8.67	2020	[64]
PEN/ITO/SnO <sub>2</sub> /perovskite/Spiro-OMeTAD/Au (active area= 0.9 cm <sup>2</sup> )	1.124	22.2	0.74	18.5	2020	[65]
PI/Cu grid/Graphene/PEDOT:PSS/Perovskite/PC61BM/ZnO/Ag	0.97± 0.02	21.5 ± 0.2	0.75 ± 0.1	15.9 ± 0.3	2020	[66]
PDMS/hc-PEDOT:PSS/AI4083/Perovskite/PCBM/PEI/hc-PEDOT:PSS/PDMS (without s-PU) (active area= 0.1 6cm <sup>2</sup> )	1.00±0.004	19.20±0.07	0.7325±0.0321	14.06±0.63	2020	[67]
PDMS/hc-PEDOT:PSS/AI4083/Perovskite/PCBM/PEI/hc-PEDOT:PSS/PDMS (with s-PU) (active area= 0.1 6cm <sup>2</sup> )	1.08±0.004	22.30±0.04	0.7758±0.0124	18.68±0.46	2020	[67]
PET/PEDOT:PSS/NiOx/Perovskite:s-GO/PCBM/BCP/Ag (active area= 1.01 cm <sup>2</sup> )	1.12	23.44	0.7830	20.56	2021	[68]
<b>PEN/ITO/HfO<sub>2</sub>/SnO<sub>2</sub>/Rb<sub>0.05</sub>Co<sub>0.05</sub>(FA<sub>0.83</sub>MA<sub>0.17</sub>)<sub>0.95</sub>Br<sub>0.05</sub>)/ Spiro-OMeTAD/Au (active area= 0.092 cm<sup>2</sup>)</b>	<b>1.148</b>	<b>24.47</b>	<b>0.8135</b>	<b>22.85</b>	<b>2021</b>	<b>[69]</b>
PET/ITO/NiOx/ CH <sub>3</sub> NH <sub>3</sub> PbI <sub>3</sub> /EVA/PCBM/ ITO/PET (active area= 0.19 cm <sup>2</sup> )	0.87±0.05	2.20±1.84	0.34±0.22	1.15±1.05	2021	[70]
EVA/PET/ITO/NiOx/ CH <sub>3</sub> NH <sub>3</sub> PbI <sub>3</sub> /EVA/PCBM/ ITO/PET/EVA (active area= 0.19 cm <sup>2</sup> )	0.92±0.04	11.47±1.55	0.30±0.19	5.15±0.97	2021	[70]
PET/EVA/PET/ITO/NiOx/ CH <sub>3</sub> NH <sub>3</sub> PbI <sub>3</sub> /EVA/PCBM/PEI/ITO/PET/EVA/PET (active area= 0.19 cm <sup>2</sup> )	0.94±0.04	18.94±0.98	0.40±0.17	10.12±0.74	2021	[70]
PET/ITO/SnO <sub>2</sub> / MAPbI <sub>3</sub> /Carbon (active area= 6 mm <sup>2</sup> )				11.11	2021	[71]
PET/ graphene-AgNWs/SnO <sub>2</sub> / MAPbI <sub>3</sub> /Carbon (active area= 6 mm <sup>2</sup> )				9.73	2021	[71]
PET/Gr/MoS <sub>2</sub> /MAPbI <sub>3</sub> /PTAA/Au (No. of Graphene layer= 1) (active area= 16 mm <sup>2</sup> )	0.88	19.90	0.6823	11.95	2021	[72]
PET/Gr/MoS <sub>2</sub> /MAPbI <sub>3</sub> /PTAA/Au (No. of Graphene layer= 2) (active area= 16 mm <sup>2</sup> )	0.91	20.92	0.7573	14.42	2021	[72]
PET Gr/MoS <sub>2</sub> /MAPbI <sub>3</sub> /PTAA/Au (No. of Graphene layer= 3) (active area= 16 mm <sup>2</sup> )	0.93	20.14	0.7487	14.02	2021	[72]



PET/Gr/MoS <sub>2</sub> /MAPbI <sub>3</sub> /PTAA/Au (No. of Graphene layer= 4) (active area= 16 mm <sup>2</sup> )	0.93	19.38	0.7289	13.14	2021	[72]
PET/ITO/Planar TiO <sub>2</sub> /TiO <sub>2</sub> nanopillars/Perovskite/Spiro-OMeTAD/Au (active area= 7.25 mm <sup>2</sup> )	0.97	20.51	0.67	13.33	2021	[73]
PET/ITO/BTF5/Perovskite/C <sub>60</sub> /BCP/Ag (active area= 0.105 cm <sup>2</sup> )	0.78 ± 0.01	21.18 ± 0.12	0.65 ± 0.02	10.88 ± 0.36	2021	[74]
PET/ITO/BTF6/Perovskite/C <sub>60</sub> /BCP/Ag (active area= 0.105 cm <sup>2</sup> )	1.12 ± 0.01	22.07 ± 0.10	0.80 ± 0.01	19.78 ± 0.33	2021	[74]
PET/ITO/PTAA/Perovskite/C <sub>60</sub> /BCP/Ag (active area= 0.105 cm <sup>2</sup> )	1.12 ± 0.01	22.35 ± 0.20	0.79 ± 0.02	20.36 ± 0.38	2021	[74]
PPFC/PET/ITO/SnO <sub>2</sub> NPs/(CH <sub>3</sub> (NH <sub>2</sub> ) <sub>2</sub> PbI <sub>3</sub> ) <sub>0.95</sub> (CH <sub>3</sub> NH <sub>3</sub> PbBr <sub>3</sub> ) <sub>0.05</sub> (FAPbI <sub>3</sub> ) <sub>0.95</sub> (MAPbBr <sub>3</sub> ) <sub>0.05</sub> /Spiro-OMeTAD/Au (PPFC 0) (active area= 0.096 cm <sup>2</sup> )	1.11	22.77	0.7354	18.59	2021	[75]
PPFC/PET/ITO/SnO <sub>2</sub> NPs/(CH <sub>3</sub> (NH <sub>2</sub> ) <sub>2</sub> PbI <sub>3</sub> ) <sub>0.95</sub> (CH <sub>3</sub> NH <sub>3</sub> PbBr <sub>3</sub> ) <sub>0.05</sub> (FAPbI <sub>3</sub> ) <sub>0.95</sub> (MAPbBr <sub>3</sub> ) <sub>0.05</sub> /Spiro-OMeTAD/Au (PPFC 80) (active area= 0.096 cm <sup>2</sup> )	1.13	23.37	0.7406	19.56	2021	[75]
PPFC/PET/ITO/SnO <sub>2</sub> NPs/(CH <sub>3</sub> (NH <sub>2</sub> ) <sub>2</sub> PbI <sub>3</sub> ) <sub>0.95</sub> (CH <sub>3</sub> NH <sub>3</sub> PbBr <sub>3</sub> ) <sub>0.05</sub> (FAPbI <sub>3</sub> ) <sub>0.95</sub> (MAPbBr <sub>3</sub> ) <sub>0.05</sub> /Spiro-OMeTAD/Au (PPFC 100) (active area= 0.096 cm <sup>2</sup> )	1.12	23.64	0.7438	19.69	2021	[75]
PPFC/PET/ITO/SnO <sub>2</sub> NPs/(CH <sub>3</sub> (NH <sub>2</sub> ) <sub>2</sub> PbI <sub>3</sub> ) <sub>0.95</sub> (CH <sub>3</sub> NH <sub>3</sub> PbBr <sub>3</sub> ) <sub>0.05</sub> (FAPbI <sub>3</sub> ) <sub>0.95</sub> (MAPbBr <sub>3</sub> ) <sub>0.05</sub> /Spiro-OMeTAD/Au (PPFC 120) (active area= 0.096 cm <sup>2</sup> )	1.11	23.51	0.7431	19.39	2021	[75]
PET/UV Resin/ITO/PTAA/(FA <sub>0.92</sub> MA <sub>0.08</sub> ) <sub>0.9</sub> Cs <sub>0.1</sub> Pb(I <sub>0.92</sub> Br <sub>0.08</sub> ) <sub>3</sub> /C60/BCP/Ag (active area= 2.25 cm <sup>2</sup> )	4.583	4.614	0.600	12.680	2022	[76]
PET/UV Resin/ITO/PTAA/(FA <sub>0.92</sub> MA <sub>0.08</sub> ) <sub>0.9</sub> Cs <sub>0.1</sub> Pb(I <sub>0.92</sub> Br <sub>0.08</sub> ) <sub>3</sub> /C60/BCP/Ag (active area= 2.25 cm <sup>2</sup> )	4.670	4.551	0.580	12.319	2022	[76]
PEN/ITO/SnO <sub>2</sub> /Perovskite/Spiro-OMeTAD/Au (active area= 0.105 cm <sup>2</sup> )	1.138	23.39	0.790	21.03	2022	[77]
PEN/ITO/Bio-IL/Perovskite/BCP/Ag (Bio-IL concentration= 0 mg/mL) (active area= 0.1 cm <sup>2</sup> )	1.09	22.09	0.7928	19.01	2022	[78]
PEN/ITO/Bio-IL/Perovskite/BCP/Ag (Bio-IL concentration= 0.03 mg/mL) (active area= 0.1 cm <sup>2</sup> )	1.11	23.46	0.7945	20.49	2022	[78]
PEN/ITO/Bio-IL/Perovskite/BCP/Ag (Bio-IL concentration= 0.05 mg/mL) (active area= 0.1 cm <sup>2</sup> )	1.11	23.50	0.8076	21.08	2022	[78]
PEN/ITO/Bio-IL/Perovskite/BCP/Ag (Bio-IL concentration= 0.07 mg/mL) (active area= 0.1 cm <sup>2</sup> )	1.10	23.73	0.7828	20.39	2022	[78]
PEN/ITO/Bio-IL/Perovskite/BCP/Ag (Bio-IL concentration= 0.09 mg/mL) (active area= 0.1 cm <sup>2</sup> )	1.09	22.69	0.7774	19.30	2022	[78]
PEN/ITO/Bio-IL/Perovskite/BCP/Ag (Bio-IL concentration= 1.01 cm <sup>2</sup> )	1.08 ± 0.01	20.68 ± 0.57	0.7702 ± 0.0167	17.35 ± 0.56	2022	[78]
<b>PET/ITO/SnO<sub>2</sub>/3D MHP /2D MHP/HTL/Au (3D perovskite= 2-BBAI) (active area= 0.049 cm<sup>2</sup>)</b>	<b>1.13 ± 0.01</b>	<b>23.1 ± 0.2</b>	<b>0.801 ± 0.0023</b>	<b>21 ± 0.8</b>	<b>2022</b>	<b>[79]</b>
PET/ITO/SnO <sub>2</sub> /3D MHP /2D MHP/HTL/Au(3D perovskite= 3-BBAI) (active area= 0.09 cm <sup>2</sup> )	1.10 ± 0.01	1.10 ± 0.01	0.796 ± 0.009	20.1 ± 0.4	2022	[79]
PET/ITO/SnO <sub>2</sub> /3D MHP /2D MHP/HTL/Au(3D perovskite= 4-BBAI) (active area= 0.09 cm <sup>2</sup> )	1.14 ± 0.02	23.1 ± 0.3	0.804 ± 0.013	21.1 ± 0.6	2022	[79]
PEN/ITO/PEDOST:PSS/NBG PVSK/C60/BCP/Cu (SnF <sub>2</sub> = 0 mol%) (active area= 0.09 cm <sup>2</sup> )	0.627±0.014	27.53±0.39	0.6922±0.0195	11.97±0.60	2023	[80]
PEN/ITO/PEDOST:PSS/NBG PVSK/C60/BCP/Cu (SnF <sub>2</sub> = 2.5 mol%) (active area= 0.09 cm <sup>2</sup> )	0.747±0.008	28.01±0.28	0.7366±0.0204	15.43±0.44	2023	[80]
PEN/ITO/PEDOST:PSS/NBG PVSK/C60/BCP/Cu (SnF <sub>2</sub> = 5.0 mol%) (active area= 0.09 cm <sup>2</sup> )	0.781±0.018	29.24±0.85	0.7261±0.0333	16.60±0.91	2023	[80]
PEN/ITO/PEDOST:PSS/NBG PVSK/C60/BCP/Cu (SnF <sub>2</sub> = 10 mol%) (active area= 0.09 cm <sup>2</sup> )	0.811±0.007	28.51±0.55	0.7561±0.0172	17.48±0.39	2023	[80]
PEN/ITO/PEDOST:PSS/NBG PVSK/C60/BCP/Cu (SnF <sub>2</sub> = 15 mol%) (active area= 0.09 cm <sup>2</sup> )	0.792±0.004	28.12±0.46	0.7182±0.0310	16.00±0.89	2023	[80]
PET/ITO/FA <sub>0.92</sub> MA <sub>0.08</sub> PbI <sub>3</sub> /Spiro-OMeTAD/Au	1.07	24.89	0.75	19.98	2023	[21]
PET/ITO/Pero-N/Spiro-OMeTAD/Au (0.5 mg mL <sup>-1</sup> ) (active area= 0.08 cm <sup>2</sup> )	1.10	24.83	0.76	20.75	2023	[21]
PET/ITO/Pero-N/Spiro-OMeTAD/Au (1.0 mg mL <sup>-1</sup> ) (active area= 0.08 cm <sup>2</sup> )	1.12	24.85	0.78	21.71	2023	[21]
PET/ITO/Pero-N/Spiro-OMeTAD/Au (1.5 mg mL <sup>-1</sup> ) (active area= 0.08 cm <sup>2</sup> )	1.13	24.82	0.76	21.32	2023	[21]
PET/ITO/Pero-I/Spiro-OMeTAD/Au (0.5 mg mL <sup>-1</sup> ) (active area= 0.08 cm <sup>2</sup> )	1.13	24.81	0.78	21.89	2023	[21]
PET/ITO/Pero-I/Spiro-OMeTAD/Au (1.0 mg mL <sup>-1</sup> ) (active area= 0.08 cm <sup>2</sup> )	1.15	24.83	0.81	23.05	2023	[21]
PET/ITO/Pero-I/Spiro-OMeTAD/Au (1.5 mg mL <sup>-1</sup> ) (active area= 0.08 cm <sup>2</sup> )	1.17	24.79	0.77	22.33	2023	[21]
PEN/ITO/TMPU/Perovskite/TMFS/ Spiro-OMeTAD/Au (TMPU concentration= 0 mM) (active area= 0.06 cm <sup>2</sup> )	1.06	22.13	70.08	16.44	2023	[22]
PEN/ITO/TMPU/Perovskite/TMFS/ Spiro-OMeTAD/Au (TMPU concentration= 2 mM) (active area= 0.06 cm <sup>2</sup> )	1.09	22.26	72.63	17.62	2023	[22]
PEN/ITO/TMPU/Perovskite/TMFS/ Spiro-OMeTAD/Au (TMPU concentration= 5 mM) (active area= 0.06 cm <sup>2</sup> )	1.12	22.32	73.65	18.41	2023	[22]
PEN/ITO/TMPU/Perovskite/TMFS/ Spiro-OMeTAD/Au (TMPU concentration= 10 mM) (active area= 0.06 cm <sup>2</sup> )	1.10	22.18	72.67	17.73	2023	[22]
PEN/ITO/TMPU/Perovskite/TMFS/ Spiro-OMeTAD/Au (TMFS concentration= 0 mM) (active area= 0.06 cm <sup>2</sup> )	1.12	22.32	73.65	18.41	2023	[22]
PEN/ITO/TMPU/Perovskite/TMFS/ Spiro-OMeTAD/Au (TMFS concentration= 2 mM) (active area= 0.06 cm <sup>2</sup> )	1.15	22.37	74.55	19.19	2023	[22]
PEN/ITO/TMPU/Perovskite/TMFS/ Spiro-OMeTAD/Au (TMFS concentration= 5 mM) (active area= 0.06 cm <sup>2</sup> )	1.16	22.38	77.27	20.06	2023	[22]
PEN/ITO/TMPU/Perovskite/TMFS/ Spiro-OMeTAD/Au (TMFS concentration= 10 mM) (active area= 0.06 cm <sup>2</sup> )	1.14	22.35	74.49	18.98	2023	[22]
PEN/PTAA/ZIF-67/Perovskite/C60/BCP/Cu (active area= 0.0805 cm <sup>2</sup> )	23.26	1.097	78.94	20.16	2023	[81]
PEN/ITO/SnO <sub>2</sub> /MAPbI <sub>3</sub> /Carbon (CNT concentration: 0 mg/mL) (active area= 0.0805 cm <sup>2</sup> )	1.01±0.01	18.57±0.34	0.6080±0.0071	11.41±0.2	2023	[82]
PEN/ITO/SnO <sub>2</sub> /MAPbI <sub>3</sub> /Carbon (CNT concentration: 0.5 mg/mL) (active area= 0.0805 cm <sup>2</sup> )	1.03±0.01	19.28±0.14	0.6315±0.0054	12.56±0.18	2023	[82]
PEN/ITO/SnO <sub>2</sub> /MAPbI <sub>3</sub> /Carbon (CNT concentration: 1.0 mg/mL) (active area= 0.0805 cm <sup>2</sup> )	1.04±0.01	20.04±0.24	0.6409±0.0064	13.39±0.16	2023	[82]
PEN/ITO/SnO <sub>2</sub> /MAPbI <sub>3</sub> /Carbon (CNT concentration: 2.0 mg/mL) (active area= 0.0805 cm <sup>2</sup> )	1.03±0.01	19.56±0.15	0.6169±0.0062	12.58±0.21	2023	[82]
PEN/ITO/SnO <sub>2</sub> /MAPbI <sub>3</sub> /Carbon (CNT concentration: 4.0 mg/mL) (active area= 0.0805 cm <sup>2</sup> )	1.02±0.01	18.16±0.21	0.5952±0.0091	10.91±0.32	2023	[82]
PMMA/PEN/ITO/SnO <sub>2</sub> /MAPbI <sub>3</sub> /Carbon (CNT concentration: 1.0 mg/mL) (active area= 0.0805 cm <sup>2</sup> )	1.05±0.01	20.85±0.23	0.6477±0.0060	14.13±0.17	2023	[82]
PET/ITO/ F-TiO <sub>2</sub> -SnO <sub>2</sub> /Perovskite/ Spiro-OMeTAD/Ag (active area= 0.049 cm <sup>2</sup> )	1.133145	24.15257	0.8225855	22.51281	2023	[83]
PET/ITO/ Cs <sub>0.08</sub> (FA <sub>0.78</sub> MA <sub>0.16</sub> )Pb(I <sub>0.84</sub> Br <sub>0.16</sub> ) <sub>3</sub> /TBAB/ Spiro-OMeTAD/Au (2 mg TBAB) (active area= 0.049 cm <sup>2</sup> ) (1000 lx)	0.918 ± 0.004	0.171 ± 0.003	0.733 ± 0.021	29.3 ± 1.1	2023	[84]
PET/ITO/ Cs <sub>0.08</sub> (FA <sub>0.78</sub> MA <sub>0.16</sub> )Pb(I <sub>0.84</sub> Br <sub>0.16</sub> ) <sub>3</sub> /TBAB/ Spiro-OMeTAD/Au (2 mg TBAB) (active area= 0.049 cm <sup>2</sup> ) (200 lx)	0.849 ± 0.007	0.031 ± 0.001	0.701 ± 0.021	23.2 ± 0.9	2023	[84]
PET/ITO/ Cs <sub>0.08</sub> (FA <sub>0.78</sub> MA <sub>0.16</sub> )Pb(I <sub>0.84</sub> Br <sub>0.16</sub> ) <sub>3</sub> /TBAB/ Spiro-OMeTAD/Au (5 mg TBAB) (active area= 0.049 cm <sup>2</sup> ) (1000 lx)	0.931 ± 0.005	0.168 ± 0.004	0.760 ± 0.018	30.5 ± 1.0	2023	[84]
PET/ITO/ Cs <sub>0.08</sub> (FA <sub>0.78</sub> MA <sub>0.16</sub> )Pb(I <sub>0.84</sub> Br <sub>0.16</sub> ) <sub>3</sub> /TBAB/ Spiro-OMeTAD/Au (5 mg TBAB) (active area= 0.049 cm <sup>2</sup> ) (200 lx)	0.861 ± 0.013	0.031 ± 0.002	0.724 ± 0.028	24.9 ± 1.7	2023	[84]
<b>PET/ITO/ Cs<sub>0.08</sub>(FA<sub>0.78</sub>MA<sub>0.16</sub>)Pb(I<sub>0.84</sub>Br<sub>0.16</sub>)<sub>3</sub>/TBAB/ Spiro-OMeTAD/Au (10 mg TBAB) (active area= 0.049 cm<sup>2</sup>) (1000 lx)</b>	<b>0.953 ± 0.004</b>	<b>0.169 ± 0.002</b>	<b>0.770 ± 0.015</b>	<b>31.6 ± 0.7</b>	<b>2023</b>	<b>[84]</b>
PET/ITO/ Cs <sub>0.08</sub> (FA <sub>0.78</sub> MA <sub>0.16</sub> )Pb(I <sub>0.84</sub> Br <sub>0.16</sub> ) <sub>3</sub> /TBAB/ Spiro-OMeTAD/Au (10 mg TBAB) (active area= 0.049 cm <sup>2</sup> ) (200 lx)	0.894 ± 0.009	0.031 ± 0.002	0.771 ± 0.012	27.0 ± 1.6	2023	[84]
PET/ITO/ Cs <sub>0.08</sub> (FA <sub>0.78</sub> MA <sub>0.16</sub> )Pb(I <sub>0.84</sub> Br <sub>0.16</sub> ) <sub>3</sub> /TBAB/ Spiro-OMeTAD/Au (20 mg TBAB) (active area= 0.049 cm <sup>2</sup> ) (1000 lx)	0.989 ± 0.007	0.097 ± 0.003	0.713 ± 0.016	17.4 ± 1.1	2023	[84]
PET/ITO/ Cs <sub>0.08</sub> (FA <sub>0.78</sub> MA <sub>0.16</sub> )Pb(I <sub>0.84</sub> Br <sub>0.16</sub> ) <sub>3</sub> /TBAB/ Spiro-OMeTAD/Au (20 mg TBAB) (active area= 0.049 cm <sup>2</sup> ) (200 lx)	0.824 ± 0.14	0.0203 ± 0.003	0.595 ± 0.127	12.2 ± 3.1	2023	[84]

## 2. Tuning efficiency of F-PSCs

### 2.1 Through material composition

A type of PV device known as a F-PTSC is a true integration with high efficiency, a low cost, and a vast potential application value. The F-PTSC's performance is studied using finite elements and wave optics theory.[80] **Figure 2a** displays an optical image of a F-PTSC device. With a champion PCE of 18.5%, corresponding to a  $J_{SC}$  of  $28.7 \text{ mA cm}^{-2}$ , a  $V_{OC}$  of 0.819 V, and an FF of 78.7%, the flexible Pb-Sn (NBG) PSC with 10 mol%  $\text{SnF}_2$  demonstrated the best performance (**Figure 2b**). According to **Figure 2c**, the  $V_{OC}$  of devices based on  $(\text{FASnI}_3)_{0.6}(\text{MAPbI}_3)_{0.4}$  showed a similar trend to that of the PLQY data. This similarity implies that the inclusion of the  $\text{SnF}_2$  additive not only improves the optoelectronic properties of the absorber material but also boosts the overall performance of the device stack. As demonstrated in **Figure 2d**, mechanical stacking of a highly efficient flexible Pb-Sn PSC with a flexible wide bandgap shows the adaptability of a four terminal (4T) F-PTSC. This method emphasizes the practicality of adaptable Pb-Sn PSCs in all-perovskite TSC applications. The champion 4T F-PTSC attained a PCE of 23.1%. The aforementioned remarkable outcome was achieved by utilizing a bottom subcell composed of Pb-Sn with an energy bandgap of 1.24 eV in conjunction with a top subcell consisting of  $\text{Cs}_{0.12}\text{FA}_{0.8}\text{MA}_{0.08}\text{PbI}_{1.8}\text{Br}_{1.2}$  with an energy bandgap of 1.78 eV (**Figure 2e**). This study presents the initial findings on developing flexible 4T all perovskite TSCs and flexible Pb-Sn NBG (1.24 eV) single junction **Figure 2f**. In another report, in order to create a self-assembled monolayer, Li, Ludong, et al.[85] combined two hole-selective compounds with carbazole cores and phosphonic acid anchoring groups. This connected the perovskite layer to a NiO nanocrystal film undergoing low-temperature processing. PET foil (125  $\mu\text{m}$  thickness) was used as the substrate due to its inexpensive cost, great optical transparency, and flexibility. A NiO nanocrystal film that has undergone solution processing was chosen as the hole transport layer (HTL) due to its suitability for low-temperature processing (below 100 °C). To boost photovoltaic performance, MB-NiO was added (**Figure 2g**).

This NiO interfaces with the perovskite layer on top. According to the reverse J-V scan, the top MB-NiO-based PSC device had an efficiency of 16.2%, 1.22 V for  $V_{OC}$ , 16.5 mA/cm<sup>2</sup> for  $J_{SC}$ , and 80.6% for FF (**Figure 2h**). It also showed a stabilized efficiency of 16.0%, outperforming the performance of the top NiO device, which had a stabilized PCE of 12.5% and a PCE of 13.5% with a  $J_{SC}$  of 15.3 mA/cm<sup>2</sup>,  $V_{OC}$  of 1.16 V, and FF of 76.1%. The PCE performance of flexible WBG PSCs (0.049 cm<sup>2</sup>) with bare NiO and MB-NiO with different MeO-2PACz molar ratios was compared using 15 devices of each type (**Figure 2i**). The central line is the median, while the box margins are the quartiles with the highest and lowest values of the distribution. The whiskers extend to display the dataset's lowest and highest possible values. Developing a molecule-bridged interface in conjunction with the tandem device structure represents a promising step toward producing exceptionally efficient F-PSCs and solar modules.

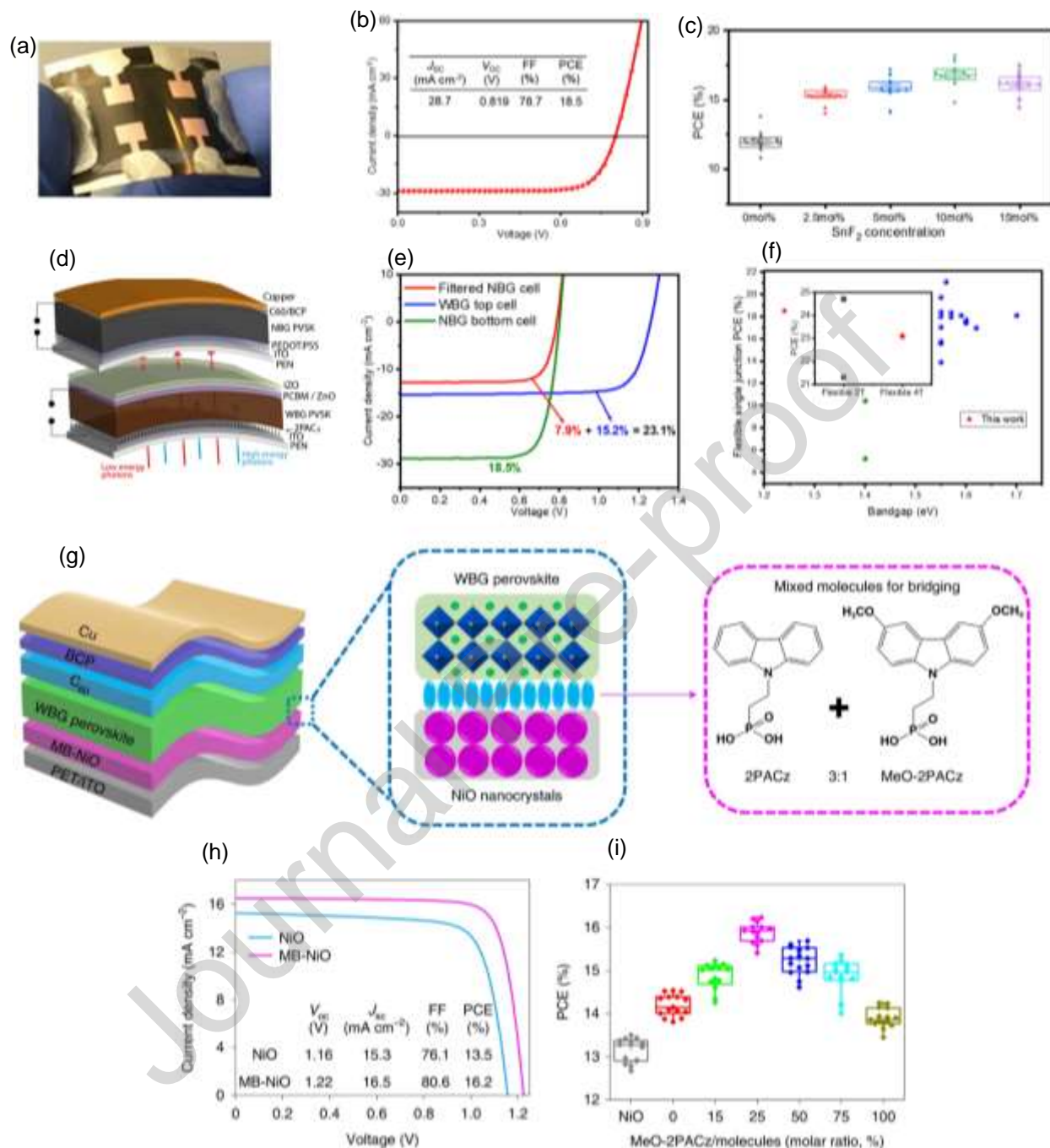


**Figure 2.** a) Structure of F-PTSC. b) The champion flexible NBG device's J-V plot. c) PCE using various  $\text{SnF}_2$  additive mol%. d) A 4T F-PTSC schematic. e) The 4T tandem configuration's subcell J-V properties. f) Plot showing the bandgap against the reported single-junction F-PTSC efficiency. The graph in the inset illustrates the reported efficiencies of F-PTSC. This study shows that red asterisks denote the device's PCE values. a–f) Reproduce with permission.[80] Copyright 2023, ACS. g) Structure of F-PSC devices. h) J-V characteristics of the MB-NiO and NiO champion devices. i) PCE performance of flexible WBG PSCs ( $0.049 \text{ cm}^2$ ) utilizing bare NiO and

MB-NiO with different MeO-2PACz molar ratios was compared using 15 devices of each type. a–f) Reproduce with permission.[86] Copyright 2022, Nature.

## 2.2 Tuning PCE with variable sunlight angles

The morphology of the Chinese dragon influences the design of 2T all-perovskite F-PTSC.[20] When simulating 2T F-PTSCs, parameter optimization is crucial. The thicknesses, optical constants, and other perovskite material properties have been obtained from the literature. A F-PTSC was physically modelled, and a schematic representation of the structure is shown in **Figure 3a**. As seen in **Figure 3b**, several F-PTSC configurations with various structural variations have been established. In order to simplify the process of creating unique configurations for the flexible tandem PV device, parametric expressions have been used. The main goal of the study is to determine how F-PTSCs with different structural configurations react to different angles of sunlight. Throughout the day, the angle  $\theta$  of incident light on the surface of the TSCs varies with respect to vertical illumination due to Earth's rotation. As a result, it is anticipated that irradiance and  $J_{ph}$  will decrease proportionately by a factor of  $\cos(\theta)$ , which stands for the effective area that receives sunlight. It is presumed that no spectral alterations occur throughout this procedure.[87] To demonstrate the broad-spectrum absorption's optical and wide-angle characteristics in F-PTSCs, light absorption and reflection characteristics of TSCs with Case 2, Case 3, Case 4, and Case 5 structures were calculated. The computations were performed at various angles and wavelengths of incident light. Furthermore, the relationship between  $J_{ph}$  and incident angle was analyzed in order to compare the performance of various F-PTSCs types with TSCs with a flat structure (Case 1) in **Figure 3c**. The combined impact of structural P and light incident angle on matched  $J_{ph}$  densities was examined (**Figure 3d**). When the wavelength, P, was increased from 100 to 1000 nm and the incident angle was decreased from 85 degrees to 0 degrees, the peak current density,  $J_{top}$ , changed from  $4.45 \text{ mA cm}^{-2}$  to  $18.80 \text{ mA cm}^{-2}$  while the bottom current

density,  $J_{\text{bottom}}$ , increased from 4.15 to 19.30  $\text{mA cm}^{-2}$ . When  $P$  is between 400 and 600 nm, and the incident angle is between 30 and 60 degrees, the  $J_{\text{ph}}$  of the upper and bottom cells exhibits a wavy pattern. The physical symmetry of  $J_{\text{ph}}$  responses can be observed in both flexible and planner structure designs when the incident angle ranges from  $-90^\circ$  to  $90^\circ$ . This phenomenon is attributed to the distinctive geometry of the F-PSC, as depicted in **Figure 3d**. The steepness of the device surface increases as  $ff$  increases. When sunlight rays reach the device's surface at an angle, the increased surface roughness results in numerous light reflections and refractions. This improved light path length inside the device enhances the photosensitivity of different layers. The device's J-V curve was determined by relating  $J_{\text{ph}}$  and  $V_{\text{oc}}$  (**Figure 3e**). The proposed technology is a highly efficient and F-PTSC with a shallow surface. The design of Fresnel reflection and its minimal dependence on the incident angle of light can be achieved by utilizing theoretical study as a reliable and practical framework. These strategies will facilitate the development of all-perovskite (F-PTSCs) as a viable alternative for future PVs.

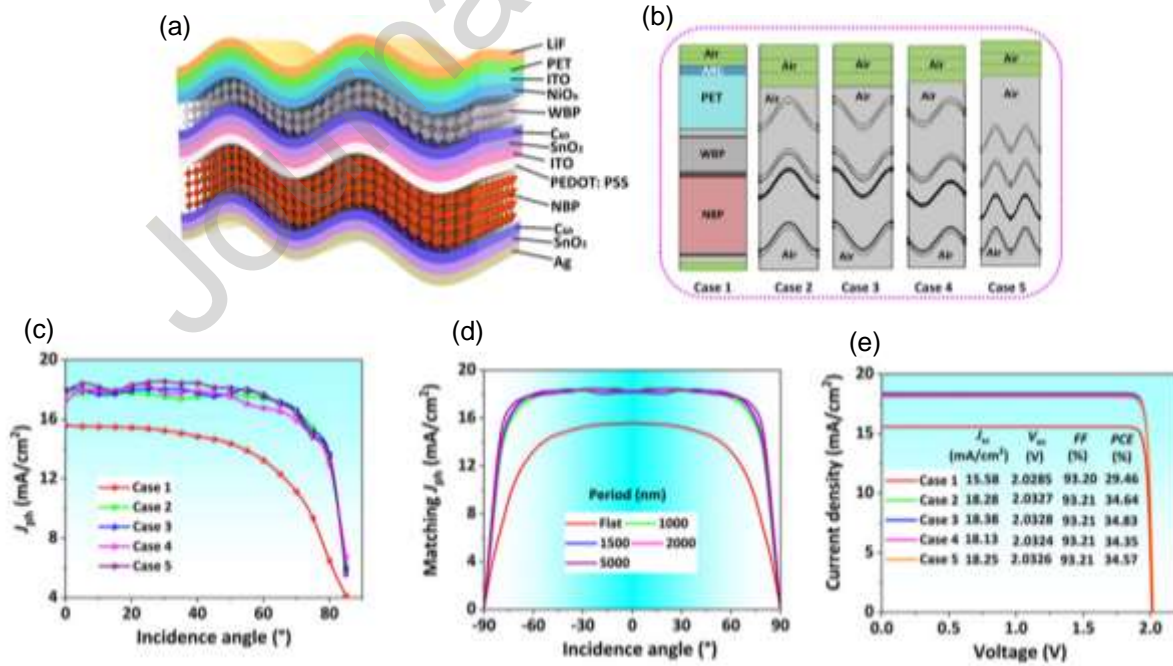


**Figure 3.** g) Diagrammatic representation of the flexible tandem PV system's structure. h) The tandem device matching's  $J_{ph}$  density changes with the incident angle ( $-90^\circ \approx 90^\circ$ ) when the period is different. i) Electrical characteristics and J-V curves of 2T flexible all-perovskite TSCs with various structural types. a–f) Reproduce with permission.[20] Copyright 2023, Wiley.

### 3. Enhanced performance through interfacial engineering in F-PSCs

In n-i-p structured PSCs, inorganic ETLs are crucial. Examples of these ETLs include  $TiO_2$  and  $SnO_2$ . In particular, the ETL in F-PSCs with a polymer substrate must adhere well to a TCO and help create a homogeneous thin film below  $150^\circ C$ .  $SnO_2$  colloidal nanoparticles are, therefore, mainly used to satisfy these needs. However, there are still areas where efficiency, coating uniformity, and TCO adhesion can be improved. To create a  $SnO_2$ – $TiO_2$  hybrid electrode, Min Je Paik et al.[19] added  $TiO_2$  nanosol, an inorganic binder, to a  $SnO_2$  colloidal solution. **Figure 4a** depicts the F-PSCs schematic and the corresponding TEM image. A hybrid  $SnO_2/TiO_2$  electrode was used to try to fabricate flexible PVSCs based on the ideal conditions found on the glass substrate. The J-V characteristics for one of the most effective F-PSCs are shown in **Figure 4b**. Under standard testing conditions, the PV parameters for the reverse scan were  $V_{oc} = 1.18$  V,  $J_{sc} = 22.53$  mA cm $^{-2}$ , and  $FF = 0.79$ , yielding an efficiency of 21.02% with minimal hysteresis. The reported PCE of these PEN-fabricated F-PSCs is among the highest. The  $V_{oc}$  value of the F-PSC increased compared to the PSC fabricated on a glass substrate. However, both  $J_{sc}$  and  $FF$  values dropped, resulting in an overall decrease in efficiency. F-PSCs are less efficient than those on glass substrates due to the ITO layer's low crystallinity and high resistance to PEN. Irrespective of the manner of bending, whether concave or convex, the PCE of F-PSCs based on  $TiO_2$ – $SnO_2$  hybrid electrodes exhibited a mere 10% reduction in initial efficiency after undergoing 500 bending cycles, even under the harsh bending radius (**Figure 4c**). On the other hand, the reduction was more significant during the concave bending phase in the F-PSC utilizing the  $SnO_2$  electrode, aligning with previous findings.[18] After undergoing 200 bending cycles, a more than 10%

reduction in the initial PCE was observed. A flexible 7 cm by 7 cm mini-module was created utilizing a hand-etched substrate. The flexible mini-module displayed a  $V_{OC}$  = 5.82 V, a  $J_{SC}$  = 4.44  $\text{mA cm}^{-2}$ , an FF = 0.64, and a PCE = 16.62%, as shown in **Figure 4d**, which was obtained with a metal mask on the active area. This finding might be used in creating effective, adaptable, large-area PSCs.

F-PSCs with a standard n-i-p architecture sometimes face limitations in their PCE due to the high resistance and significant flaws present in the low-temperature produced metal oxide ETLs. Zhang, Linghui, et al.[83] have presented a study on amorphous F-doped  $\text{TiO}_x$  (F- $\text{TiO}_x$ ) caulked crystalline  $\text{SnO}_2$  composite ETL's electron transport loss between metal oxide nanocrystallines. According to previous research, this technique improves metal oxide mobility and passivates perovskite-ETL interfacial defects. **Figure 4e** displays the schematic representation of the planar F-PSC, which consists of n-i-p-type layers. The J-V characteristics of the champion F-PSCs based on the control  $\text{SnO}_2$  and composite ETLs are shown in **Figure 4f** in both the reverse and forward scans. The inset lists their specific PV parameters, including  $J_{SC}$ ,  $V_{OC}$ , FF, and PCE. The PCE (reverse scan) for the F-PSC based on the control  $\text{SnO}_2$  ETL was 19.68%, the  $J_{SC}$  was 23.07  $\text{mA cm}^{-2}$ , the  $V_{OC}$  was 1.12 V, and the FF was 76.30%. Comparatively, the F-PSC's  $V_{OC}$ ,  $J_{SC}$ , and FF with composite ETL have all been enhanced to 1.13 V, 24.57  $\text{mA cm}^{-2}$ , and 81.66%, respectively, yielding a record PCE of 22.70%. The possibility of F-PSCs meeting forthcoming practical applications is contingent upon their mechanical reliability and operational stability. Repeated cyclic-bending fatigue tests were conducted to assess the mechanical reliability at ambient temperatures (20% RH, 25 °C). The smallest tension-only bending radius (R), as shown in the inset of **Figure 4g**, is 5 mm. Figure 8g shows the PCE trend as a function of the number of bending cycles.  $\text{SnO}_2$  and composite ETL-based F-PSCs had good mechanical stability after 1000 cycles.



The composite ETL-based F-PSCs, however, show advantages in bending resistance as the bending test progresses; after 4000 cycles, the experimental device retained 82.11% of its initial efficiency (from 22.30% to 18.31%), whereas the control SnO<sub>2</sub> ETL-based device has decreased to 42.37% of its initial efficiency (from 19.54% to 8.28%). The operational stability of unencapsulated F-PSCs based on control SnO<sub>2</sub> and composite ETLs was then tested under normal settings, with PCE recorded every hour.

Yi, Zijun, et al. increased SnO<sub>2</sub> conductivity and minimized SnO<sub>2</sub>/perovskite interface defects using 1-[3-(trimethoxysilyl)propyl]urea (TMPU).[22] **Figure 4h** shows the flexible device's architecture with TMPU and TMFS interfacial modification layers and TMFS's molecular composition. The modified flexible device produces F-PSCs treated with varied TMFS concentrations to assess PV performance enhancement efficiency (Figure 4i). The champion F-PSCs modified with 10 mM TMFS have a  $J_{sc}$  of 22.38 mAcm<sup>-2</sup>, a  $V_{oc}$  of 1.16 V, an FF of 77.27% and a PCE of 16.44%, compared to 16.44% without the interface modification layer. **Figure 4j** shows that the target device (0.013) has a lower HI value than the control device (0.11). In contrast to the control device, the target device demonstrates remarkable resistance to bending, as it retains 91.3% of its original PCE. Silane coupling agents are strategically added to both interfaces to promote interfacial contact and toughness in F-PSCs. The findings above provide evidence that implementing dual-interface engineering enhances the overall stability of flexible devices. More importantly, dual-interface designing improves device stability, especially bending resistance. Dual-interface engineering can help commercialize high-performance F-PSCs.

F-PSCs need high PCE, long-term stability, and mechanical reliability to be commercially viable. Stacked 2D/3D perovskites can theoretically enhance F-PSCs' mechanical robustness and PCEs. Due to the complex surface interactions involved, controlling the growth of 2D perovskites

on 3D perovskites in terms of morphologies, growth sites, and mechanical properties is difficult. Yan, Ying, et al. found that the polarity of X-bromobenzylamine salts ( $X = 2, 3$ , and  $4$ ) and air moisture affect how quickly 2D perovskites develop on 3D perovskites and what processes they occur. [79] The n-i-p structure of the F-PSC is shown in **Figure 4n**. PCE data of F-PSCs with pure 3D, trans-GBs 2, 3, and 4-BBAI-based 2D/3D MHPs are shown in **Figure 4o**. They were derived from J-V characteristics in the forward (F,  $J_{sc}$  to  $V_{oc}$ ) and reverse (R,  $V_{oc}$  to  $J_{sc}$ ) scanning directions. As seen in **Figure 4p**, the F-PSCs achieved a maximum efficiency of 22.1% (reverse scan) based on the 4-BBAI/ $FA_{x-1}MA_1PbI_3$  trans-GBs 2D/3D MHP. The F-PSC displayed a PCE of 21.8% in forward scans and 22.1% in backward. The mechanical characteristics of the F-PSCs were then thoroughly studied. MHP film's main residual stress is tensile from the thermal expansion coefficient differential between MHP and ITO substrates. It is widely reported that, in the context of F-PSCs, convex bending (tension) poses a greater risk of damage (crack formation) to the MHP films compared to concave bending (compression). Further cracks will block the longitudinal transfer of light-generated charges, creating irreparable PCE damage and long-term instability in the subsequent bending phase. The primary objective of this study is to investigate the effectiveness of the 2D MHP in mitigating tensile stress cracks and improving the mechanical dependability of MHP films and associated devices. 4-BBAI-based trans-GBs 2D/3D devices show remarkable bending tolerance, which retains 80% of the initial efficiency after 8000 cycles. Without a 2D MHP capping layer, the control F-PSC's PCE is 20% lower. 2BBAI devices sustain 55% and 39% of their initial PCEs, making them mechanically stronger than 3BBAI devices. The F-PSCs fabricated utilizing this approach have demonstrated remarkable resilience to bending stresses, with noteworthy PCEs reaching a remarkable 22.1% (certified). The current technique is thought to have facilitated the rapid manufacture of F-PSCs. However, further investigation is

required to understand the underlying mechanisms, including the selectivity of the reaction at the molecular level and the specific channel through which moisture induction occurs.

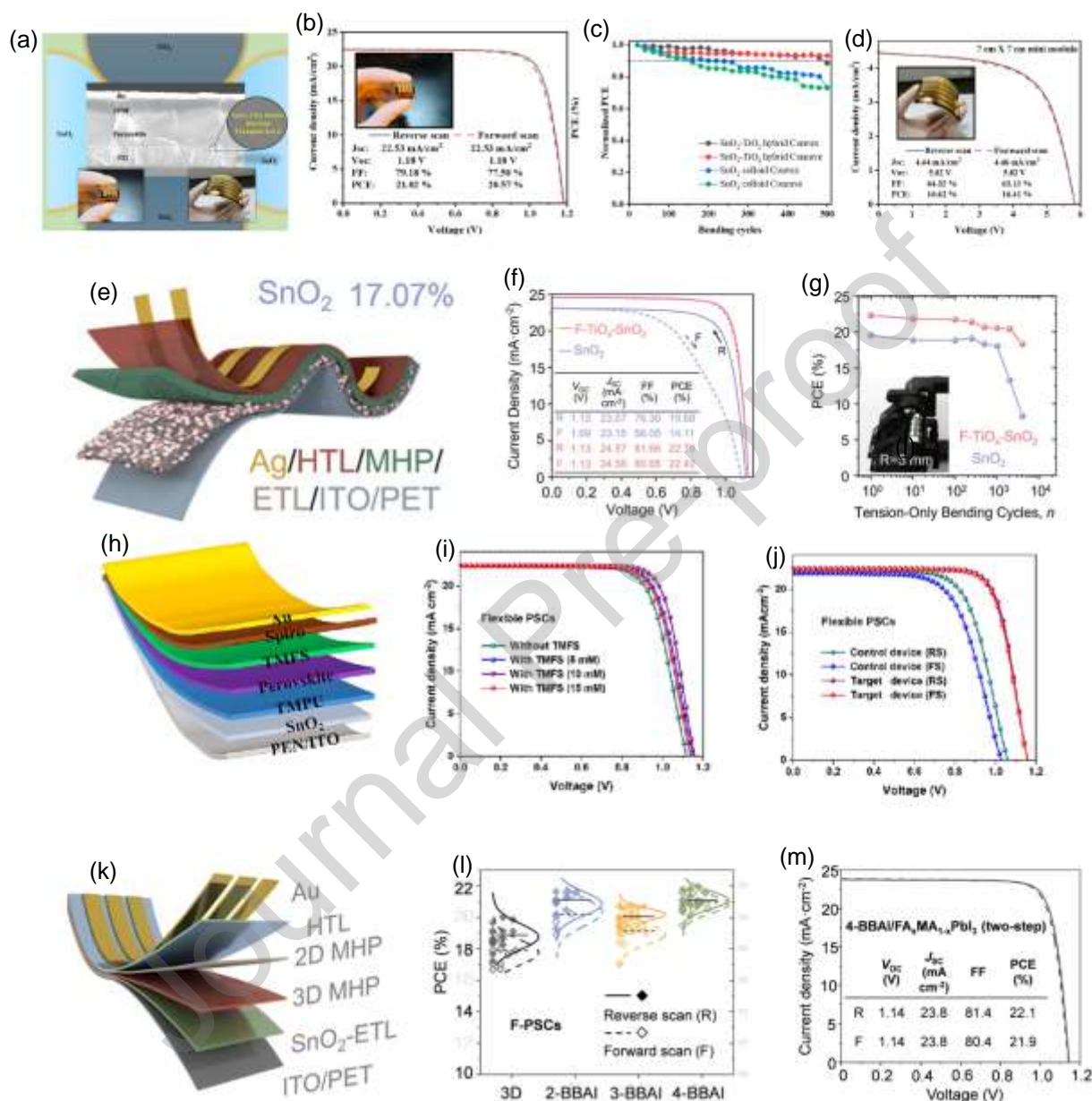


**Figure 4.** a) F-PSCs schematic and corresponding TEM image. b) J-V characteristics for the champion F-PSC, Insets: photovoltaic parameter for backward and forward scans and the fabricated device picture. c) The efficiency of a system demonstrates variability as the number of bending cycles increases, with a fixed bending radius of 5 mm. d) J-V characteristics of the manually etched mini-module built on a flexible substrate (a picture of the mini-module is included in the inset). a–d) Reproduce with permission.[19] Copyright 2022, ACS. e) The n-i-p architecture F-PSC improved composite ETL for F-TiO<sub>x</sub> and SnO<sub>2</sub>. f) J-V plots for the F-PSCs device's best performance, with forward (F) sweep and reverse (R) sweep from 0 to 1.2 V. g) The PCE of

unencapsulated F-PSCs is analyzed with the number of tension-only bending cycles ( $R = 5 \text{ mm}$ ). e–g) Reproduce with permission. [83] Copyright 2023, Wiley. h) Flexible device architecture with dual interface modification layers. i) The J–V curves of flexible  $\text{SnO}_2/\text{TMPU}$  devices with varying TMFS modification concentrations. j) Flexible devices' J–V response was measured under FS and RS conditions. h–j) Reproduce with permission.[22] Copyright 2023, Elsevier. k) Illustrates the structure of the n–i–p F-PSC. l) Forward and reverse scan of F-PSCs with and without 2D MHP capping layers. m) J–V curves. k–m) Reproduce with permission.[79] Copyright 2022, RSC.

#### **4. Stability in F-PSCs**

Environmental and mechanical stability are currently two of the most crucial issues in investigating F-PSCs. Protecting PSCs from moisture, UV rays, temperature changes, and chemical deterioration is necessary to ensure their environmental stability. However, mechanical stability is essential for their use in flexible and wearable applications, necessitating resistance to bending and stretching and strong layer adhesion. The practicality and dependability of F-PSCs for a wide range of applications, from renewable energy to flexible electronics, must be advanced by addressing these issues.

##### **4.1 Environmental stability**

F-PSC research and development must take environmental stability into account. Environmental elements like moisture, humidity, UV rays, temperature changes, and chemical exposure can harm these cells. Researchers are currently developing encapsulation techniques and materials that shield the perovskite layer from moisture and UV deterioration to guarantee long-term performance. Additionally, initiatives are being made to improve their chemical and thermal stability. This is crucial for the real-world use of F-PSCs in various situations, such as outdoors and in harsh environments, where they must continuously maintain their effectiveness and dependability.

F-PSCs are the ideal complement to conventional silicon solar cells in applications requiring portable power. The residual tensile strain, intrinsic brittleness, and high defect density along

perovskite grain boundaries make practical standards unsatisfactory, compromising these materials' mechanical, operational, and environmental stabilities. A meticulously designed cross-linkable monomer, TA-NI, has been developed to tackle the abovementioned issues by incorporating dynamic covalent hydrogen, disulphide bonds, and ammonium functionalities.[21] Cross-linking acts as "ligaments" on perovskite grain boundaries. These "ligaments" of elastomers and 1D perovskites reduce mechanical stress and residual tensile strain in 3D perovskite films while passivating grain boundaries and enhancing moisture resistance. In particular, the elastomer's dynamic self-healing ability repairs mechanical cracks in the perovskite layer caused by bending. At ambient temperature, the TA-NI elastomer, which exhibits exceptional stretchability, interacts with uncoordinated  $\text{Pb}^{2+}$  ions through its Lewis-base S atoms. This interaction enables Pero-I film self-healing of bending cracks and perovskite film mechanical tension release. (**Figure 5a**). Therefore, introducing "ligaments" at the grain boundaries may enhance the perovskite film's mechanical and environmental stability. **Figure 5b** illustrates the photovoltaic characteristics of PSCs utilizing different perovskite layers. The  $J_{sc}$ ,  $V_{oc}$ , FF, and PCE values for the F-PSCs based on the Pero-C film are  $24.89 \text{ mA cm}^{-2}$ , 1.07 V, 0.75, and 19.98%, respectively. The flexible Pero-I device delivers a maximum efficiency of 23.05% and displays improved  $V_{oc}$  and FF of 1.15 V and 0.81, respectively. After forming the 1D/3D perovskite heterostructure, the defects present at the interface between the grains were successfully mitigated, resulting in enhanced hole extraction efficiency. This led to these noticeably higher  $V_{oc}$  and FF. The  $1.004 \text{ cm}^2$  Pero-I device attained a PCE of 20.87%, a  $V_{oc}$  of 1.14 V, and an FF of 0.74. The recorded values for the devices mentioned above, Pero-N and Pero-C, significantly improve compared to their respective maximum PCEs of 19.01% and 16.57% (**Figure 5c**). The highest efficiencies for large ( $1 \text{ cm}^2$ ) and small-area F-PSCs have been reported (**Figure 5d**).



**Figure 5.** a) Diagram illustrating Pero-I's self-healing mechanism. b) small-area and c) large-area J-V characteristics of the champion n-i-p planar flexible solar cells. Devices are shown in the inset. d) PCE distribution of the F-PSCs in the area (PCE > 18%). e) Unencapsulated F-PSCs based on Pero-I, Pero-N, and Pero-C were subjected to a stability test at MPP using standard testing conditions at N<sub>2</sub> atmosphere. f) An overview of the F-PSCs' complete device performance with PCEs greater than 22.5%. a–f) Reproduce with permission.[21] Copyright 2023, Wiley.

Metal-halide perovskites are a lightweight, highly efficient PV material with many potential uses. Nevertheless, the stability of these devices is sometimes affected by numerous external influences in real-world scenarios, posing a particular challenge for flexible devices. Qiao, Feiyang, and his colleagues have conducted a study on the deterioration of F-PSCs, focusing on two prominent factors: optical and mechanical stress.[92] Surprisingly, the degradation process increases when these elements coexist simultaneously. A thorough analysis reveals that the primary factors leading to the failure of this device are the mismatch and charge buildup occurring at the interfaces. According to theoretical simulations, the primary microscopic cause of the device's instability is carrier-localization behaviour, strongly linked to lattice distortion. The finding severely limits the longevity of F-PSCs and other internal strain-sensitive devices, which cannot be passivated or encapsulated. According to theoretical studies, physical modulations like external electric fields may reduce this effect. This study improves understanding of the mechanisms that degrade realistic rigid and F-PSCs and makes it easier to find solutions. As shown in **Figure 6a**, mechanical stress was purposefully created by repeatedly bending the chosen devices. This experiment used the device without mechanical bending and with a PEAI passivated control device. Analyzing the reference device, it was decided to build more light-sensitive devices and remove the passivation layer to increase the photodegradation effect. Furthermore, applying mechanical ageing strategies to control samples reveals stress-dominated degradation in these devices. This study investigates the impact of combined optical and stress-induced degradation processes on devices lacking a passivation layer subjected to 1000 bending cycles. The four cases

are shown in **Figure 6a**. It is crucial to emphasize that all samples were continuously illuminated for 1000 hours. First, standard J-V characterizations were used to evaluate the devices' performance in **Figure 6 b's** illumination from one sun. Other samples showed various deterioration modes regarding  $V_{OC}$ ,  $J_{SC}$ , and FF losses compared to the control devices. This shows that the device design method above can separate external stimuli' individual and cooperative impacts. The statistical PCE of L.S.I. devices decreased by 69.4% (**Figure 6c**), whereas the reduction was only 9.6% for the control samples. L.S.I. devices lost 26.3% more performance than L.I. (11.9%) and S.I. (31.2%) devices. This discovery implies that the two factors combined made certain collaborative processes evident. Previous investigations have shown that continuous bending to the device causes  $J_{SC}$  and FF loss, thus increasing series resistance. This suggests that the sample's  $J_{SC}$  and FF values of the S.I. and L.S.I. should exhibit similarity.[93] The corresponding values, which unexpectedly fell below this expectation, showed that the synergetic degradation effect impacts other variables besides series resistance. Furthermore, **Figure 6d** shows the temporal progression of efficiency throughout extended aging, with all efficiencies normalized using the original values for each scenario. The mechanically bent devices experienced a significant decline in stability. External stress led the passivated device (S.I. samples) to lose 20.6% of its efficiency in 200 hours and then continuously drop, while the non-passivated (L.S.I. samples) experienced a short-circuit failure after losing 37.1%. S.I. devices retained 69% of their initial PCE, indicating that passivation's protection is ineffectual against synergetic effects. This illustrates that modern technology struggles to choose interfacial passivation chemicals to improve device stability and efficiency.[94-96] Overall, this research may help us better understand how PSCs degrade in challenging conditions and encourage the creation of flexible, high-performance perovskite devices for various uses.



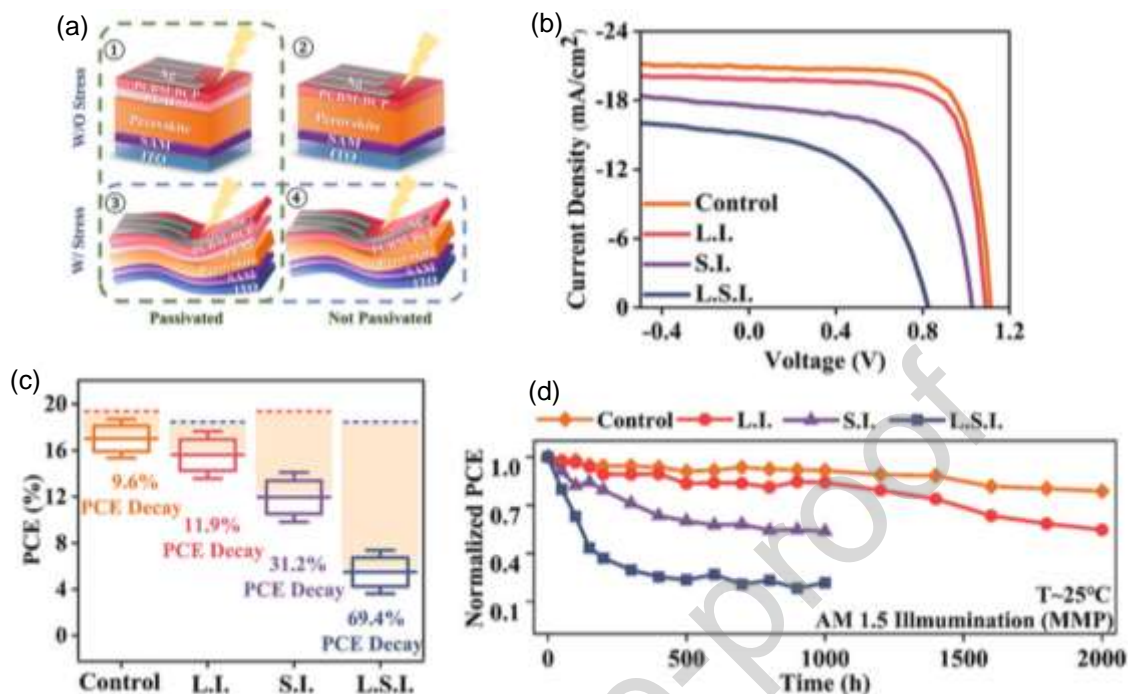


**Figure 6.** a) The specific sample composition and associated aging plans. ① a passivation layer-equipped control device. ② A device with light influence (labelled "L.I.") that lacks a passivation layer. ③ device with a stress-influenced passivation layer (labelled "S.I. ") bent 1000 times. ④ device without a passivation layer affected by light and stress and bent 1000 times. b) The designed devices' compared J-V curves were aged for 1000 hours. c) Box diagram representing the samples' efficiency distribution. d) The devices under continuous illumination's long-term PCE tracking curve. e) Different bend cycle times. a–e) Reproduce with permission.[92] Copyright 2023, Wiley.

Both of the most important interfaces in F-PSCs are subjected to mechanical reinforcement. A self-assembled monolayer (SAM) interface forms between the ETL and 3D MHP thin film. Second, an in situ-grown LD MHP capping layer connects the 3D-MHP thin film to the HTL. Dai, Zhenghong, and colleagues measured and modelled the interfacial mechanical properties.[77] The optoelectronic and mechanical properties of the two interfaces are improved holistically due to this rational interface engineering. High PCE of 21.03% (with reduced hysteresis), enhanced operational stability (1000 h lifetime at 88% initial PCE retained), and improved mechanical dependability are unique to dual-interface-reinforced F-PSCs. **Figure 7a** shows the dual-interface-reinforced F-PSC concept. **Figure 7b** shows "champion" F-PSC's forward (F) and reverse (R) J–V responses. The reverse scan data showed that all photovoltaic parameters gradually increased



**Figure 7.** a) Design of the dual-interface-reinforcement F-PSC architecture shown schematically. b) J-V responses of "champion" F-PSCs. c) EQE and integrated J<sub>sc</sub> spectra from "champion" F-PSCs in the atmosphere. d) Control, SAM, and SAM+LD F-PSCs normalized PCE over time (hourly PCE recordings under continuous 1-sun with MPP tracking, N<sub>2</sub> atmospheric flow, and 45 °C temperature). a–d) Reproduce with permission.[77] Copyright 2022, Wiley.

The low adhesion at the brittle HTL-perovskite interface contributes to the instability of inverted (p-i-n) structured devices. Dou, Jie, et al.[81] used inverted structured cells in the zeolitic imidazolate framework-67 (ZIF-67) to enhance the adhesion at the interface and extend the device's lifetime. **Figure 8a** shows the configuration of the flexible p-i-n inverted device. Through forward and reverse scanning, the device's J-V characteristics were evaluated. In **Figure 8b**, the F-PSCs treated with ZIF-67 showed better PCE of 20.16%, with a J<sub>sc</sub> of 23.26 mA cm<sup>-2</sup>, a V<sub>oc</sub> of 1.10 V, and an FF of 0.74 compared to the reference. After 200 seconds of illumination, the steady-state efficiency output could be obtained by maintaining a bias close to the MPP (0.92 V), resulting in a stabilized photocurrent of 21.38 mA cm<sup>-2</sup> (see inset of **Figure 8b**). The MPP tracking operational stability of unencapsulated F-PSCs was investigated under 1 sun illumination in an N<sub>2</sub> atmosphere (**Figure 8c**). The reference device's efficiencies fell below 40% over less than 500 hours, whereas the ZIF-67 treated F-PSC device maintained 80% of its initial efficiency over 1200 h. The device with bias showed a shorter lifetime due to the electrode's diffusion there. The results of the stability test indicate that incorporating ZIF-67 led to an enhancement in the light stability of F-PSCs. This type of multifunctional material offers a novel opportunity for expediting its commercialization and has the potential to be utilized in various applications such as LEDs and other optoelectronics. To reduce the coffee-ring effect when printing perovskite modules, Fan, Baojin, and colleagues introduce a bionic interface layer (Bio-IL) of NiOx/levodopa, which is inspired by the bio-glue of barnacles.[78] Since meniscus printing has a wide variety of applications and is suitable for developing roll-to-roll (R2R) technology, it is used to produce large-area F-PSCs. The schematic diagram that exhibits correlation can be observed in **Figure 8d**.

The substrate must enable rapid and uniform perovskite colloidal particle deposition and three-phase contact line pinning. Barnacles can stick to the animal's (i.e., whale, turtle, etc.) skin because they exude levodopa-containing bio-glue. (**Figure 8d middle part**). The strong interaction of levodopa with other surfaces makes bio-glue stick well. Adding levodopa to uniformly pinned perovskite colloidal particles on the NiOx layer with bio-glue creates sticky Bio-IL. The right part of Figure 6f shows the chosen inverted device structure: PEN/ITO/Bio-IL/perovskite/PCBM/BCP/Ag. **Figure 8e** (flexible device) displays the J-V curves of the best devices, and the insets contain corresponding images. The flexible devices produce a PCE of 18.16%, a  $J_{SC}$  of  $21.59 \text{ mA cm}^{-2}$ , a  $V_{OC}$  of 1.08 V, and an FF of 77.94%. Rigid  $1.01 \text{ cm}^2$  inverted PSCs based on NiOx provide the best photoelectric performance ( $22.97 \text{ mA cm}^{-2}$ , 1.11 V, 79.81%, and 20.30%). [99] PCE evolution across active areas is shown in **Figure 8f**. Reference device PCE falls dramatically with increased active area (34.95% at  $1.01 \text{ cm}^2$ ). The coffee-ring effect reduced PCE by causing numerous perovskite defects. When the effective area is  $1.01 \text{ cm}^2$ , Bio-ILA devices have 10.34% lower PCE loss (light blue region). Reduced trap state density in printed perovskite film with better uniformity is due to PCE's negative trend with the rising active area being considerably corrected. Bio-IL's effect on F-PSC mechanical stability was first investigated by bending the device (3 mm bending radius). **Figure 8g** shows how flexible devices' PCE evolution over time is tracked. The reference device approaches failure after 1400 hours of storage; however, the Bio-IL gadget can maintain 70% of the initial PCE. A dense and homogenous printed perovskite coating based on Bio-IL makes the rigid PSC 80.17% stable after 1400 h of storage. offers fresh insight into the variables and mechanisms influencing the perovskite film's quality during the meniscus printing process and valuable, practical knowledge for producing high-performance flexible solar energy sources.

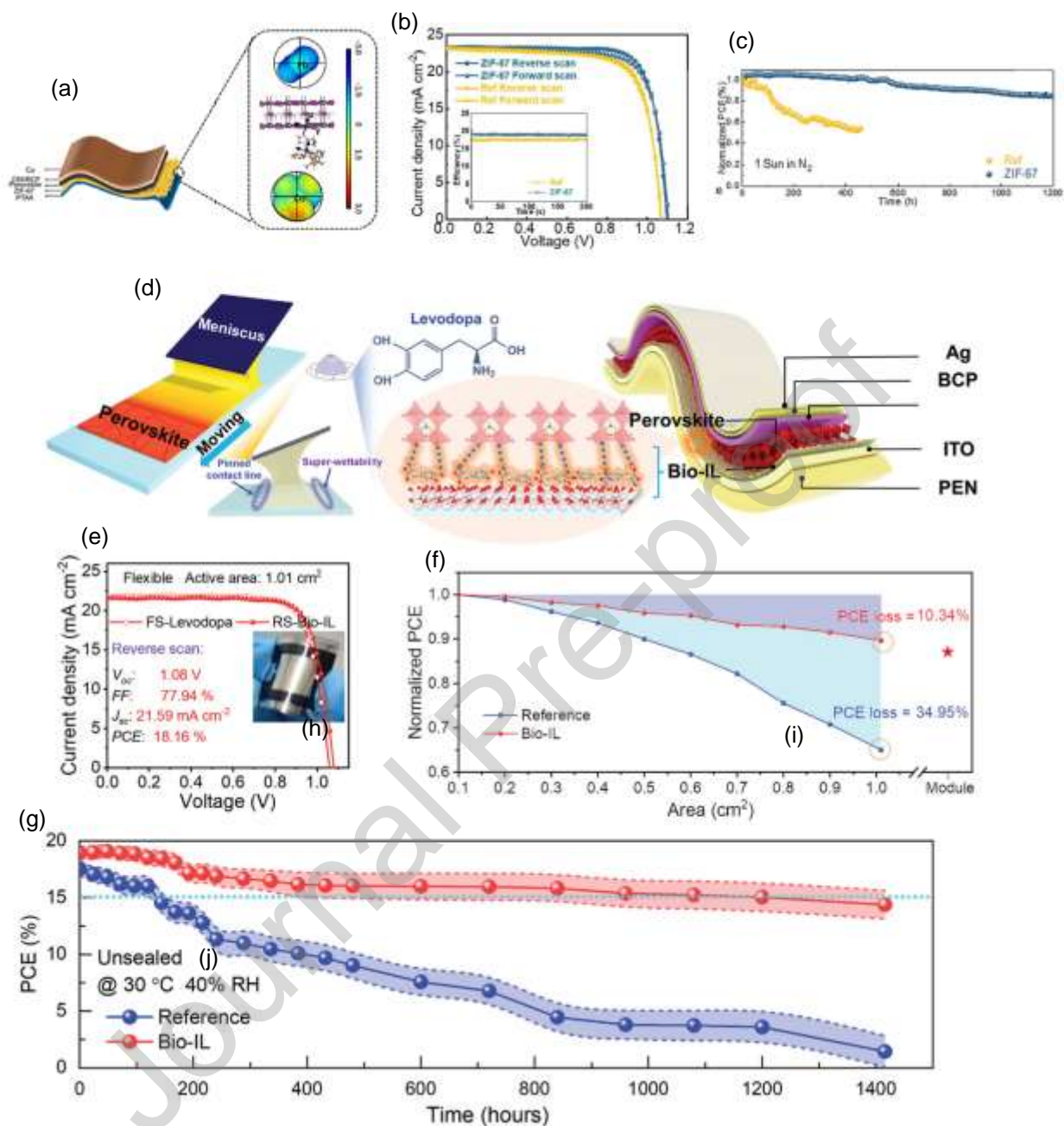


**Figure 8.** a) Flexible perovskite solar cell ZIF-67 schematic. b) J-V characteristics of the F-PSC before and after ZIF-67 treatment. Inset: The photocurrent in steady-state was measured at a bias voltage close to the peak power point, specifically 0.88 V before ZIF-67 treatment and 0.92 V after ZIF-67 treatment. c) when bent repeatedly with a radius of 6 mm. a–c) Reproduce with permission.[81] Copyright 2023, Elsevier. d) Schematic of printed F-PSCs. Left: Diagram of the meniscus coating for perovskite film, with a 5 mm/s blade movement. Middle: Mechanisms modelled after biological systems and at the right perovskite device design. e) J-V curves of reference and Bio-IL substrates for large-area flexible PCs. A photograph of a F-PSC is shown in the inset. f) 1.01 cm<sup>2</sup> active area for Bio-IL substrates-based F-PSC with normalized PCE

evolution. g) F-PSCs ( $0.1 \text{ cm}^2$ ) based on reference and Bio-IL substrates underwent PCE evolution over time. d–g) Reproduce with permission.[78] Copyright 2022, Wiley.

#### 4.2 Mechanical stability

PSCs are being developed, and mechanical stability is a key factor. For these cells to be long-lasting and perform consistently, they must be able to withstand a variety of mechanical stresses, such as bending, stretching, and physical impacts. To strengthen the mechanical integrity of F-PSCs, researchers are concentrating on creating flexible substrates, improving encapsulation processes, and improving adhesion between different layers. This is crucial for applications in flexible electronics, solar-integrated clothing, and wearable electronics where the solar cells must adapt to various shapes and withstand daily use.

Ludong Li et al. mix two hole-selective compounds with carbazole cores and phosphonic acid anchoring groups to build a self-assembling monolayer and attach perovskite to a low-temperature NiO nanocrystal sheet. [85] In the tandem cells, the device configuration was inverted, with the following layers: PET/ITO/MB-NiO/wide-bandgap perovskite/ $\text{C}_{60}$ /ALD- $\text{SnO}_2$ /Au/PEDOT:PSS/narrow-bandgap perovskite/ $\text{C}_{60}$ /BCP/Cu (**Figure 9a**). BCP specifically refers to bathocuproine. During the reverse scan, the top flexible TSC using MB-NiO achieved a remarkable efficiency of 24.7%. It demonstrated an aperture area of  $0.049 \text{ cm}^2$ ,  $V_{\text{OC}}$  of 2.00 V, a  $J_{\text{SC}}$  of  $15.8 \text{ mA/cm}^2$ , and a FF of 78.3% (**Figure 9b**). Tests on the durability of bending were performed on flexible TSCs that were either NiO or MB-NiO-equipped. The flexible TSC with MB-NiO continued to function properly even after 10,000 bending cycles, each with a 15 mm bending radius (**Figure 9c**). However, TSCs using unmodified NiO only retained 72% efficiency after 10,000 bending cycles. The front wide band gap (WBG) subcell's molecule-bridged interface between the hole transport layer (NiO) and the perovskite is primarily responsible for the enhanced bending durability seen in tandem devices. It is important to note that the NiO and MB-NiO

devices' other interfaces and layers are the same. There are several reasons why the molecule-bridged interface improves bending stability. SAMs may increase adhesion toughness at the fragile WBG perovskite-NiO interface, improving mechanical robustness. The molecule-bridged interface's structure can also serve as a stress-buffering layer, shielding the delicate perovskite film from bending-related damages. This is corroborated by the experiments' findings that the WBG films deposited on MB-NiO after bending did not exhibit any discernible crack formation. The tandem device structure and the molecule-bridged interface are poised to open up new paths for developing solar cells and PSCs that are incredibly efficient.

In situ crosslinking using bis((3-methyloxetan-3-yl) methyl) thiophene-2,5-dicarboxylate was investigated by Wu, Yeyong, et al.[100] during the growth of perovskites. This compound's crosslinking temperature and coordination capacity allowed for precise, real-time control of perovskite quality. **Figure 9d** shows a possible schematic outlining the grain growth process made possible by crosslinking. With different bending radii, the perovskite film in its pristine state showed poor resistance to deformation, which led to noticeable fractures (as shown in **Figure 9e, h**). On the contrary, the bends and deformations in the perovskite-MOTC film (MOTC: bis((3-methyloxetan-3-yl) methyl) thiophene-2,5-dicarboxylate) were significantly reduced (**Figure 9f**). This was made possible by the larger grain size that was obtained and the adaptable properties of the organic MOTC compound attached to the grain boundaries. In contrast, as shown in **Figure 9g**, the perovskite-COETC film showed no signs of damage or fractures during the bending tests. This finding suggests that the elastic properties of the crosslinked OETC effectively dissipated the applied stress and reduced deformations. This finding is consistent with the perovskite-COETC film's lower Young's modulus. These findings provide important information about improving the mechanical toughness and performance of F-PSCs. The proposed method of in situ crosslinking-



assisted perovskite film growth has great potential for improving the manufacturing of F-PSCs that satisfy the requirements of practical applications.

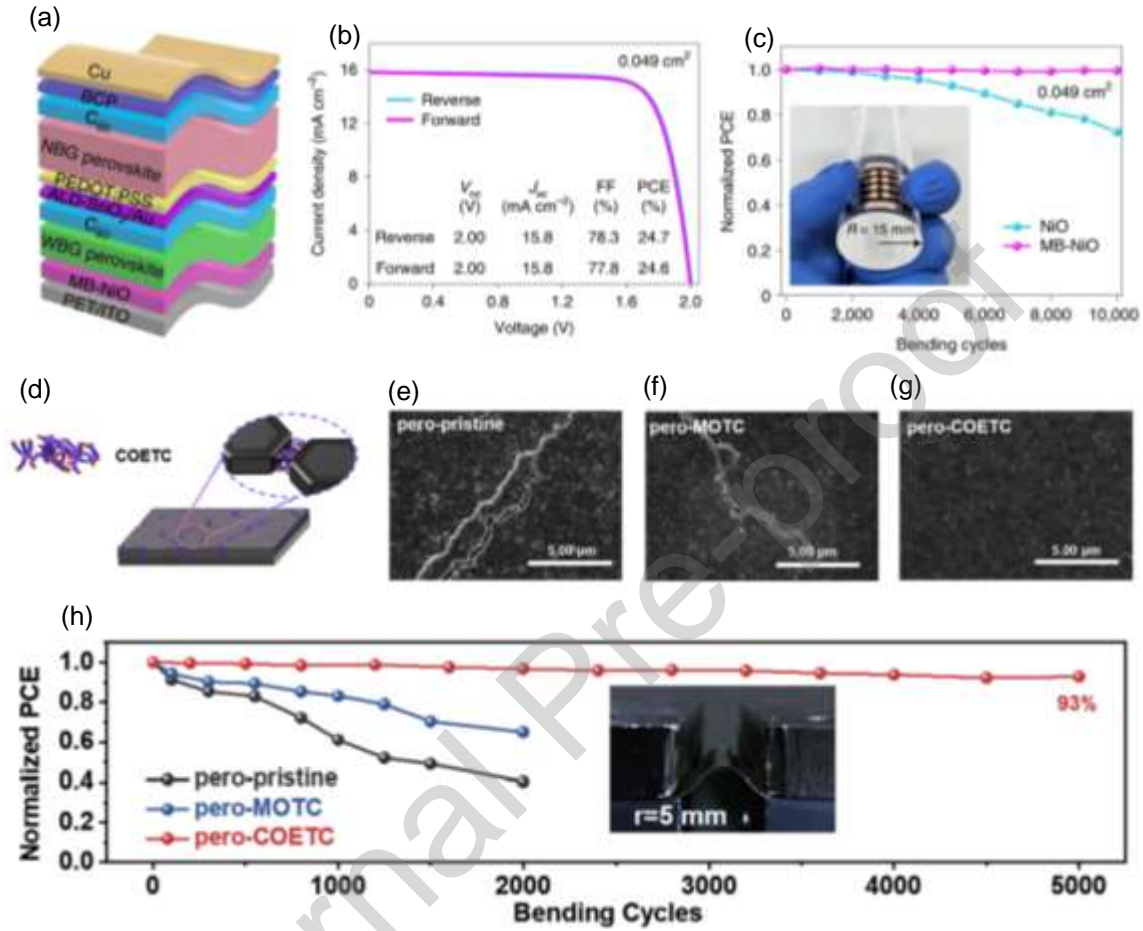


**Figure 9.** a) The structure of the device. b) J-V curve. c) Flexibility studies on TSC with a 15 mm bending radius composed of NiO and MB-NiO. Initial PCEs for flexible TSC based on NiO and MB-NiO are 22.0% and 24.6%, respectively. a–c) Reproduce with permission.[85] Copyright 2022, Nature. d) Crosslinked OETC schematic. e to g) The perovskite films are shown in three different states in SEM images taken from a top-view perspective: perovskite-pristine, perovskite-MOTC, and perovskite-COETC following 2,000 cycles of bending with a 5 mm bending radius. h) The flexible perovskite solar cells' PCE was plotted against the quantity of bending cycles with a 5 mm bending radius. d–h) Reproduce with permission.[100] Copyright 2023, Elsevier.

Yang, Lu, et al.[7] created flexible devices with the next-generation HADI-SnO<sub>2</sub> ETL in order to increase the potential applications for this material: PET/ITO/SnO<sub>2</sub> or HADI-SnO<sub>2</sub>/FA<sub>0.9</sub>Cs<sub>0.1</sub>PbI<sub>3</sub>/Spiro-OMeTAD/A (**Figure 10a**). The J-V curves of the champion flexible devices are shown in **Figure 10b**. The control PSC has a PCE of 20.18% at J<sub>sc</sub> of 24.45 mA/cm<sup>2</sup>,



$V_{oc}$  of 1.11 V, and FF of 74.11%. The device produces the highest PCE and  $V_{oc}$  for F-PSCs—22.44%, 1.17 V, respectively and  $J_{sc}$  of 24.64 mA/cm<sup>2</sup>, and FF of 78.16%—after receiving the histamine diiodate (HADI) treatment. HADI-treated F-PSCs were tested for operational stability during repetitive bending at various curvature radii (R) to determine their suitability as a power source in wearable electronics. The amount of bending in the device increased and the film's damage worsened with a decrease in the value of R from 400 to 2 mm. Nevertheless, as shown in **Figure 10c**, the device lost 10% of initial efficiency even after being bent at R = 2 mm. The production of high-quality SnO<sub>2</sub> using this universal surface passivation method is efficient and can benefit rigid and F-PSCs, LEDs, and various other optoelectronic applications.

Liu, Zhike, et al.[32] presented the ground-breaking design of ultrathin and F-PSCs incorporating transparent electrodes made of graphene for the first time. **Figure 10d** illustrates the F-PSCs device structure: PET/graphene/P3HT/CH<sub>3</sub>NH<sub>3</sub>PbI<sub>3</sub>/PC<sub>71</sub>BM/Ag. **Fig. 10e** shows a F-PSC on 0.175 cm-bending surfaces. **Figure 10f** shows how well a flexible, bending-durable PSC performs. After 500 bending tests (0.175 cm bending radius), the F-PSC's PCE declined 14% due to decreased  $J_{sc}$ . The control devices' perovskite layer, graphene electrode, and Ag top electrode shape changed little following bending testing. This device performance stability is a crucial element. Surprisingly, as shown in **Figure 10g**, the decline in  $J_{sc}$  is directly proportional to the decline in PCE. During the bending tests, FF and  $V_{oc}$  showed only minor variations, indicating that the graphene electrode's resistance remained constant. Due to its brittle nature, the perovskite layer cracks under mechanical stress, causing device deterioration. These faults can result from poor carrier transport, additional traps in the active layer, and lower  $J_{sc}$ . In order to understand the performance degradation more thoroughly. The primary cause of the deterioration of thick devices is the cracking of the metal electrodes and the perovskite active layers as a result of the increased

strain brought on by bending. Therefore, using ultrathin substrates, which can lessen the strain felt during bending tests, is a viable strategy to improve bending stability. This study paves the way for the incorporation of transparent graphene electrodes into high-efficiency F-PSCs and offers bright prospects for a variety of flexible optoelectronic devices based on graphene.

Gong, Oh Yeong, et al.[98] report that van der Waals stacking (vdWS) produces uniform, extraordinarily crystalline perovskite films on flexible substrates employing a consistent heat transmission mechanism during annealing. [101] **Figure 10g** shows a schematic of the vdWS-induced lift-off process, which improved heat transport and produced a high-quality perovskite layer. **Figure 10h** shows the J-V characteristics of the champion device, which has a  $0.14\text{ cm}^2$  active area and operates under illuminations of 1 sun. These panels' inset display the stabilized power output. Notably, with little hysteresis, the device's PCE was 22.54% during reverse scans and 22.10% (1 sun) during forward-scans. F-PSCs underwent cyclic bending tests with a 5 mm bending radius to confirm their mechanical durability. The devices treated with vdWS/OLA/vacuum, as shown in **Figure 10i**, displayed strong mechanical stability, maintaining an average of 81% of their initial PCE after 1000 bending cycles. However, following the same number of bending cycles, vdWS-treated devices' average PCE dropped to 65% of their initial performance. The bending stress resulted in numerous surface cracks on the vdWS perovskite film, as seen. The vdWS/OLA/vacuum perovskite film, in contrast, lacked these cracks. According to this finding, the OLA (oleylamine) passivation layer is essential in reducing bending stress within the perovskite film, which ultimately improves its mechanical stability. The bending stress resulted in numerous surface cracks on the vdWS perovskite film, as seen. The vdWS/OLA/vacuum perovskite film, in contrast, lacked these cracks. According to this finding, the OLA (oleylamine)

passivation layer is essential in reducing bending stress within the perovskite film, which ultimately improves its mechanical stability.

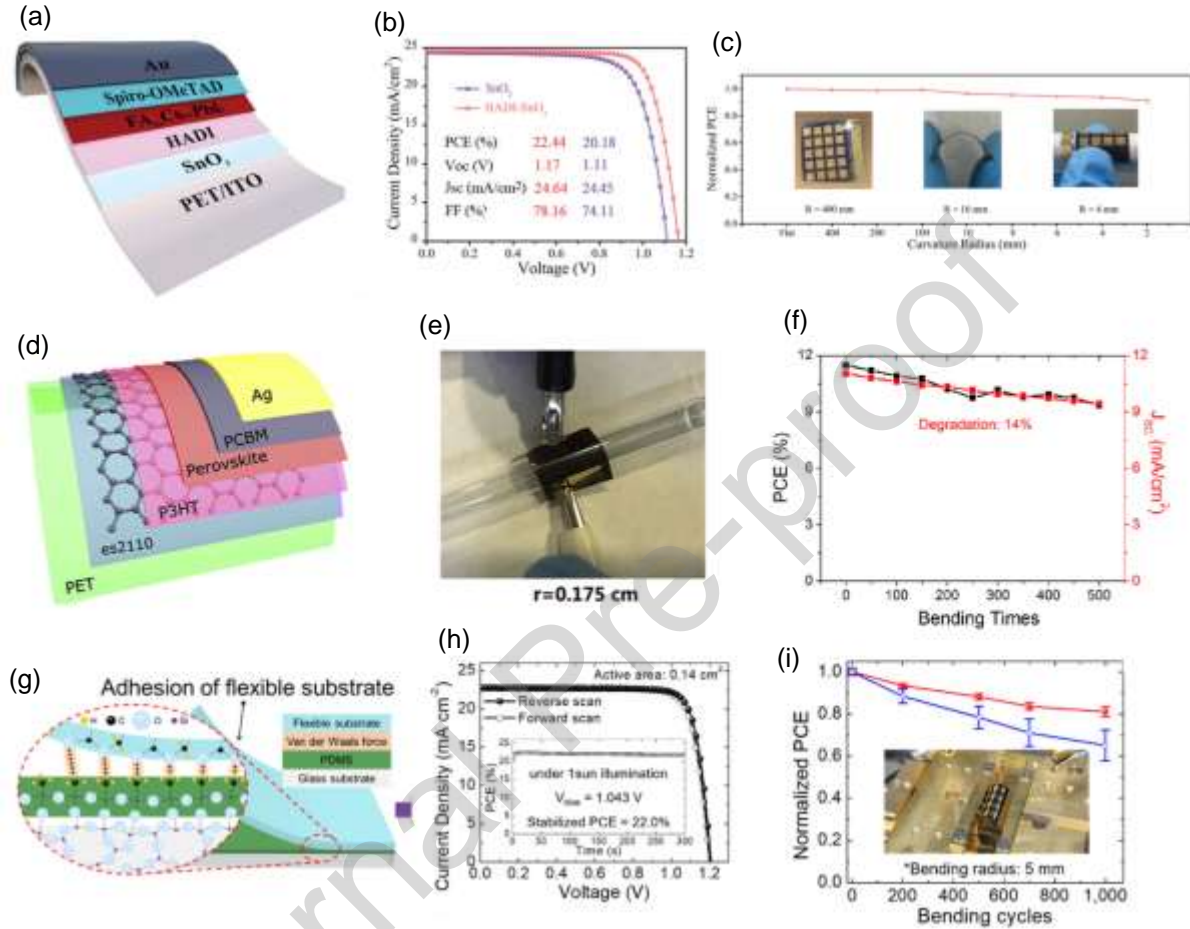


**Figure 10.** a) Flexible device architecture. b)  $J$ - $V$  curves. c) Curved normalized PCE from flat to  $R = 2$  mm. a–c) Reproduce with permission.[7] Copyright 2022, Wiley. d) Diagram of a schematic. e) A F-PSC attached to surfaces with bending radius 0.175 cm is shown in a photograph. f) Functions of bending radius for the PSC's PCE and  $J_{sc}$ . e–f) Reproduce with permission.[32] Copyright 2016, Elsevier.

Using the pentylammonium acetate (PenAAc) molecule to alter the interface between the perovskite and the hole transport layer, Gao, Danpeng, et al.[102] have created a flexible inverted PSC that is highly effective and stable. Inverted F-PSCs were made using the following materials in the following order: polyethylene naphthalenediide/ITO/PTAA/passivation layer/perovskite/C60/2,9-dimethyl-4,7-diphenyl-1,10-phenanthroline/Ag. This device configuration is shown in **Figure 11a** (modified to use PenAAc as an example). The best-

performing device, which used PenAAc to improve it, shows a significant increase in PCE, achieving a remarkable value of 23.68%. A higher  $J_{sc}$  of 24.85 mA/cm<sup>2</sup>,  $V_{oc}$  of 1.17 V, and a high FF of 81.33% are in conjunction with it. Notably, as shown in **Figure 11b**, this device shows little hysteresis. Mechanical bending performance tests were carried out under specific conditions where flexible solar cells might need to bend while operating. **Figure 11c** shows the differences in efficiency that resulted from mechanically bending flexible devices (with an aperture area of 0.08 cm<sup>2</sup>) at various curvature radii. The flexibility of the PenAAc-modified flexible device does not significantly degrade as the bending radius grows smaller. Even at 2 mm radius, it maintains 98% of its initial efficiency, compared to 96% for the control device. This study emphasizes interface modification's role in improving flexible perovskite PV mechanical stability and efficiency.

Methylammonium succinate, a brand-new, multipurpose organic salt, was added to the perovskite film by Li, Minghao, et al.[103] By strengthening grain boundaries and reducing strain, this incorporation helped to reduce microstrain and the amount of defects present. It is possible to increase the mechanical durability of perovskite films thanks to the MS molecule's distinctive bilateral structure, which is capable of strong binding with grain boundaries and microstrain relaxation. Based on MS-perovskite and PEN/ITO substrates, we developed F-PSC devices, as shown in **Figure 11d**. The top-performing F-PSC' J-V curves and PV metrics both with and without the addition of MS is shown in **Figure 11e**. With a reverse scan PCE of 23.6%, a  $J_{sc}$  of 24.72 mA/cm<sup>2</sup>,  $V_{oc}$  of 1.151 V, and a FF of 82.93%, the winning MS-flexible-PSC excelled. This performed better than the champion control device's 21.6% PCE. The device that performed best had little hysteresis and had a PCE of 23.2% in the forward scan. F-PSC devices' mechanical stability and efficiency were assessed using a continuous bending test. After 10,000 bending cycles (with a bending radius of 6 mm), the control F-PSC gradually saw its efficiency drop to 60% of

the initial PCE. The MS-flexible-PSC, in contrast, kept about 85% of its initial PCE (as shown in **Figure 11f**). This suggests that the modified devices will be more mechanically durable. MS-flexible-PSC's mechanical stability is due to strengthened grain boundaries and relaxed microstrain, which minimized perovskite fracture and defect formation. To reduce microstrain, a variety of novel molecules with comparable supramolecular interactions, such as hydrogen bonds, coordination, and halogen bonds, can be created. The performance and stability of F-PSCs could be improved further as a result, making it easier to adopt these power sources more widely.

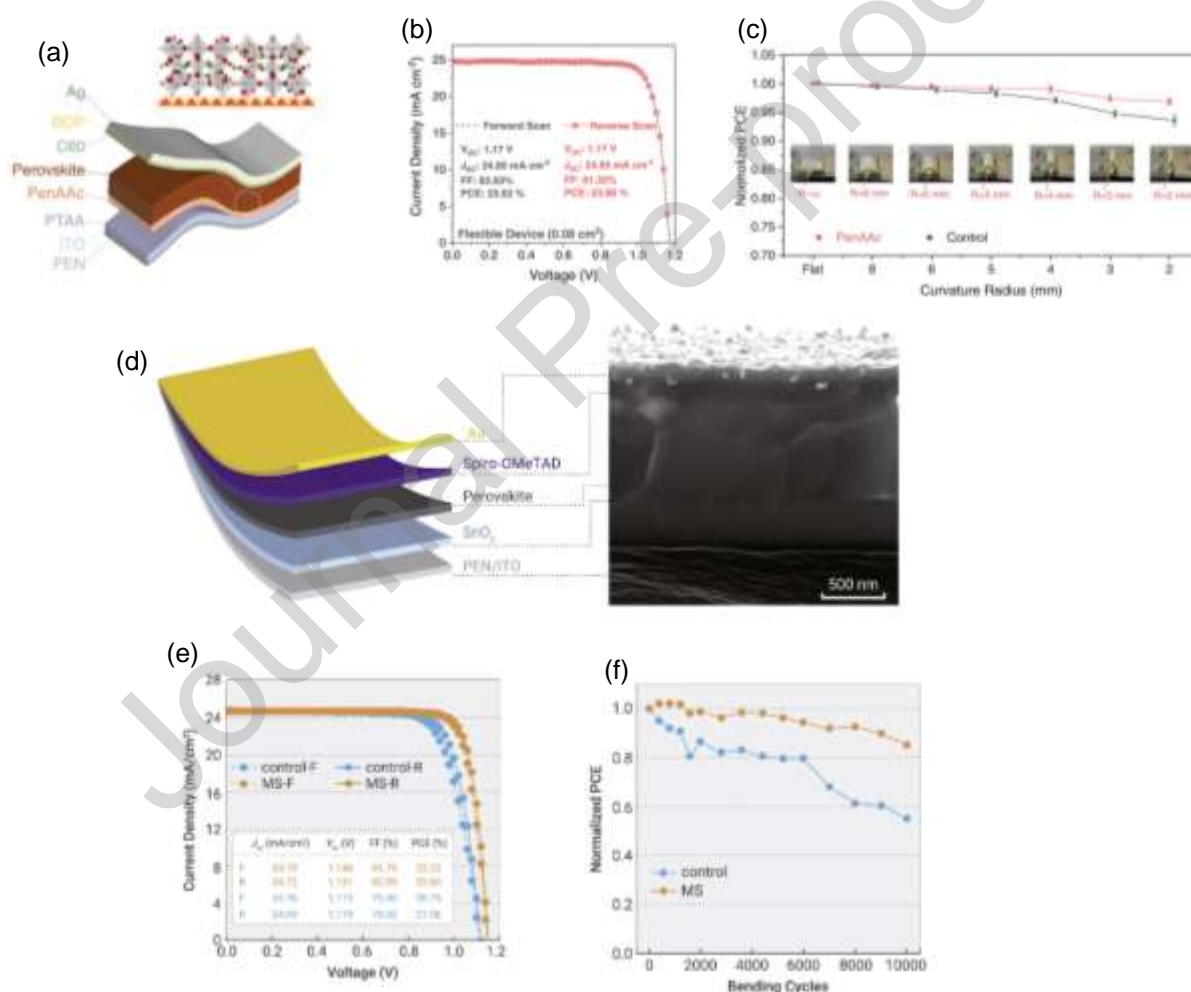


**Figure 11.** a) The device's schematic. b)  $J$ - $V$  curves. c) Normalised mean PCE of vdWS and vdWS/OLA/vacuum devices after 1000 cycles of 5 mm bending. a-c) Reproduce with permission.[32] Copyright 2022, ACS. d) Device schematic illustration. e)  $J$ - $V$  curves. f) During mechanical bending tests with varying curvature radii, F-PSCs (0.08 cm²) experienced PCE variance. d-f) Reproduce with permission.[32] Copyright 2023, Wiley. r) The F-PSC's cross-

sectional SEM image and device structure. s) *J-V* curves. t) The F-PSCs' bending stability ( $R = 6$  mm, 30% relative humidity,  $25^{\circ}\text{C}$ ). d–f) Reproduce with permission.[103] Copyright 2022, Elsevier.

PSCs made of carbon without a hole transport material (HTM) are well known for being strong contenders for real-world applications. Nevertheless, developing efficient flexible HTM-free carbon-based PSCs (C-PSCs) is restricted by the inadequate mechanical bonding between the perovskite layer and the carbon electrode and the limited light transmittance of flexible substrates. Adding a PMMA antireflection layer on PEN/ITO substrates promotes light absorption and inserts CNTs into carbon electrodes and perovskite material to improve the bond at the perovskite/carbon interface. Li, Siqi, et al.[82] produce flexible HTM-free C-PSCs with enhanced light-trapping capabilities and better flexibility. Previous studies have shown the beneficial effects of CNTs on the extraction and transfer of charges at the interface between perovskite and carbon. Additionally, incorporating CNTs has been shown to enhance the flexibility of these devices. The schematic of a F-PSC is shown in **Figure 12a**. The *J-V* characteristics of all the fabricated devices are shown in **Figure 12b**. A PCE of 11.81% (reverse scan) is shown by the best control device. The device's normalized PCEs after 1000 bends with bending radii varying from 13 mm to 5 mm are shown in **Figures 12c** and **12d**, respectively. At a 13 mm bending radius, the PCEs of the devices remain nearly unchanged. However, the control device's PCE reduces dramatically after 1000 bending cycles, along with its bending radius. 93%, 72%, 61%, and 41% of the control device's initial PCE remain after 1000 bending cycles at 13, 10, 7, and 5 mm radius. Perovskite films using CNTs have better-bending stability at all radii. After 1000 bend cycles with 13, 10, 7, and 5 mm radii, CNTs and antireflection devices retain 98%, 90%, 84%, and 71% of their initial efficiency.

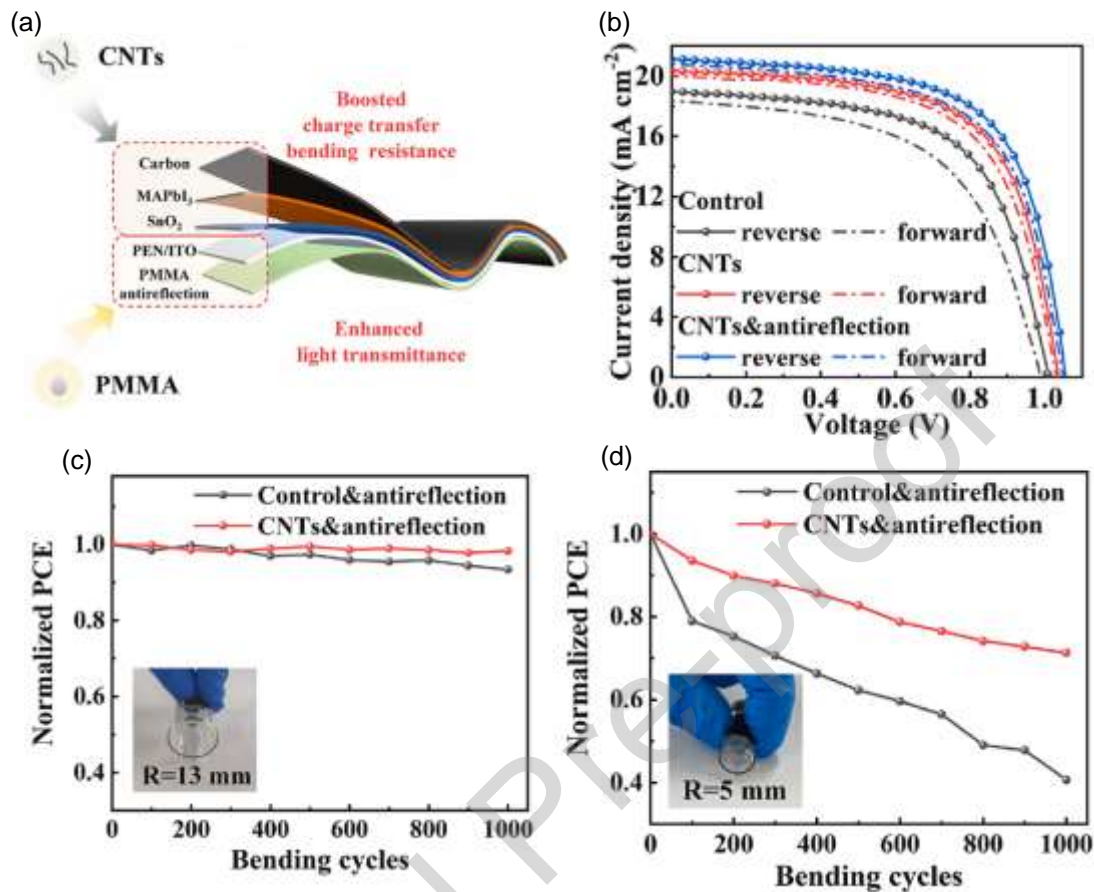


**Figure 12.** a) Flexible perovskite solar cell schematic. b) J-V curve of flexible C-PSCs under different bending radii: c) 13 mm, d) 5 mm, as a function of bending cycles. a–d) Reproduce with permission.[82] Copyright 2023, Elsevier.

PSCs that bend and stretch are lightweight and can be used on curved surfaces. In contrast to other plastic substrates, such as PET has emerged as the material of preference. PET is a crucial component of PV because it is stable and much more affordable. Zeynab Skafi et al.[84] demonstrate highly effective f-PSCs on PET using a dual low-temperature (100 °C) fabrication approach. The researchers achieved efficiencies of 28.9% by first increasing the bandgap (42% improvement) by anion mixing the lead-containing perovskite composition (replacing I with Br). Subsequently, they further enhanced the efficiencies by 26% through interfacial engineering utilizing tetrabutylammonium bromide (TBAB). **Figure 13a** presents a schematic representation of the investigated F-PSC architecture and a TBAB structural diagram. In **Figure 13b**, the box

diagram illustrates the PCE of devices featuring two distinct compositions of Br atoms operating under an illuminance of 200 lux. These devices lack an interfacial layer between the perovskite material and Spiro-MeOTAD. The next step of incorporating TBAB revealed a significant improvement in PCE, attaining a value of  $27.0 \pm 1.9\%$  under an illumination intensity of 200 lx. The synergistic effects of interfacial engineering (+26%) and compositional engineering (+42%) have, therefore, resulted in a significant improvement in performance of 92% in relative terms at these illumination levels. The emphasis is on determining the impact of TBAB incorporation. **Figure 13c, d** illustrate the J-V curves and output efficiencies of the champion F-PSC for control and TBAB modification, as evaluated under LED illumination at 200 and 1000 lx. The highest efficiency for cells was 28.9% at 200 lx (MPD =  $23.3 \mu\text{W cm}^{-2}$ ) and 32.5% at 1000 lx (MPD =  $127.8 \mu\text{W cm}^{-2}$ ). However, the best PCE for the cells without TBAB was 27.6% (MPD =  $108.4 \mu\text{W cm}^{-2}$ ) and 22.8% (MPD =  $18.4 \mu\text{W cm}^{-2}$ ) at 200 and 1000. The samples were not enclosed and kept in the dark. They were then measured at a 1000 lx illuminance level (**Figure 13e**). Following 118 days, it was observed that the devices subjected to TBAB treatment exhibited a remaining average PCE of 72% relative to their initial value. In contrast, the control cells displayed a significantly lower PCE of 29%. All PV parameters declined after 118 days of aging, with FF showing the most pronounced decline. **Figure 13f** shows the experimental setup showcasing the assessment of the bending radius, measuring approximately 1.8 cm, for the unencapsulated TBAB-passivated devices. These devices are subjected to an illuminating LED lamp with an intensity of 1000 lx. A fully TBAB-treated device with one bend is shown in the inset. Following a total of 1000 bending cycles with a bending radius of 18 mm, it is observed that the TBAB-passivated F-PSC exhibits outstanding bending stability, as it retains more than 80% of its initial PCE. This performance improvement, made possible by low-temperature techniques and



the technology's adaptability, can expand the possibilities for using light harvesting to power smart wearable, portable, and IoT electronics inside buildings.

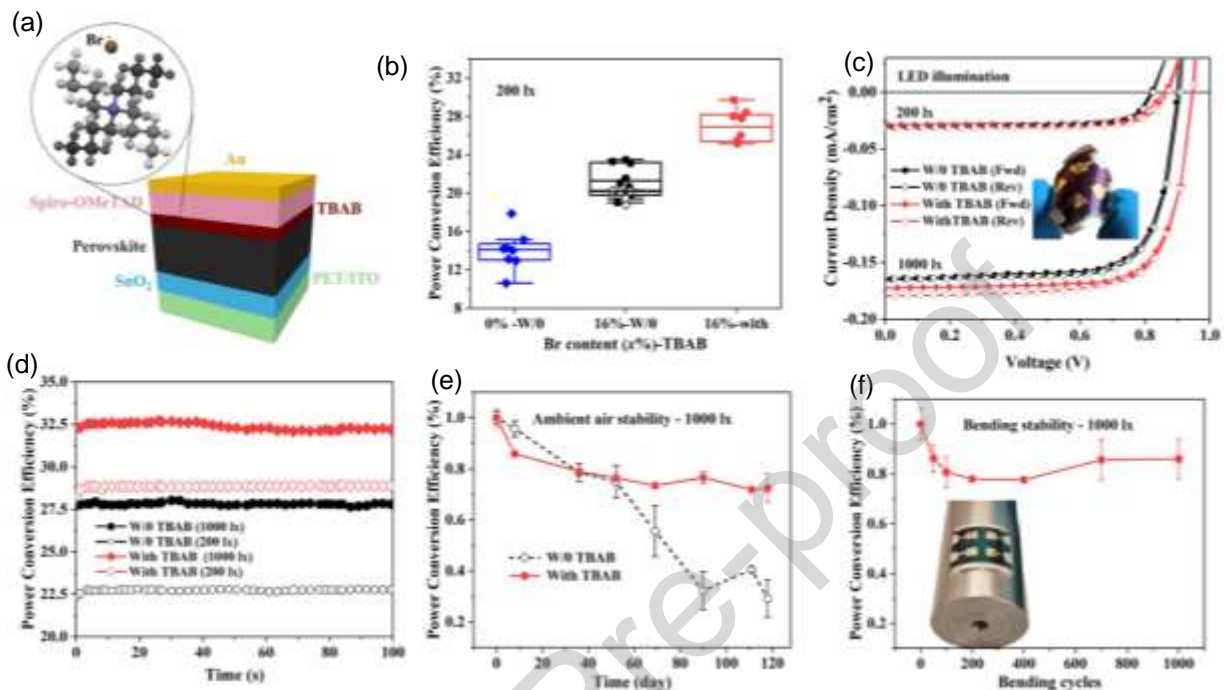


**Figure 13.** a) Diagrammatic representation of the studied FPSC architecture and the TBAB structure. b) Charts of the PCE. c) The J-V characteristics at the forward and reverse scans under an LED lamp at 200 and 1,000 lx (active area = 0.09 cm<sup>2</sup>) with and without TBAB treatment. A 2.5 x 2.5 cm<sup>2</sup> flexible sample is shown in the inset. d) Stabilized efficiency (MPP-tracking) with and without TBAB treated F-PSC under LED illumination (200 and 1000 lx), e) With and without TBAB treated F-PSC passed the ambient air stability test (ISOS-D1) under LED illumination (at 1000 lx). f) Unencapsulated TBAB-passivated devices were subjected to a 1.8 cm bending radius bend test while illuminated by a 1000 lx LED lamp. The entire TBAB-treated device is shown in the inset with one bend. a–f) Reproduce with permission.[84] Copyright 2023, Wiley.

## 5. Summary and prospects

The ability of F-PSCs to combine the adaptability of flexible substrates with the efficiency of perovskite materials is attracting a lot of attention. This extensive review explores the rapidly developing field of F-PSC research and presents a variety of innovative setups and approaches. All of these projects highlight a strong desire to improve the adaptability, durability, and affordability of PSCs—an essential goal in order to smoothly incorporate them into the mainstream energy system. The review describes in detail significant developments in several areas of F-PSC

technology. These include novel strategies extracted from various reports, like optimizing F-PSC efficiency, enhancing performance via interfacial engineering, and testing stability in the face of mechanical and environmental stresses. The various lines of investigation highlight the researchers' steadfast commitment to the continued development of F-PSCs. As F-PSCs develop, these technological advancements have the potential to drastically alter the renewable energy landscape and bring us one step closer to the widespread adoption of flexible and sustainable solar solutions.

The search for new materials will take center stage in F-PSCs in the upcoming years. Researchers are prepared to investigate non-toxic alternatives, organic-inorganic hybrid materials, and alternative perovskite compositions. The goal is to raise PSCs further regarding their effectiveness, stability, and environmental sustainability. These cutting-edge materials will improve PSC performance while advancing their eco-friendliness, a vital component of upcoming solar technologies.

The creation of F-PSCs will incorporate sustainability throughout every step of the process. The solar industry will increasingly adopt sustainable practices, such as minimizing waste production, using eco-friendly fabrication methods, and using less energy and other resources during production. This dedication to environmentally friendly manufacturing is consistent with the more general objectives of minimizing the adverse effects of renewable energy technologies. Beyond production, efforts are made to lessen F-PSCs' environmental impact. Recyclability and end-of-life management will be essential factors. Researchers will work to establish effective recycling procedures and create recyclable PSCs. In addition to reducing electronic waste, this strategy makes it possible to recover and reuse valuable materials, promoting a circular economy for solar technologies.

The F-PSC industry will work to minimize its environmental impact at every stage as part of the sustainability agenda. Comprehensive life cycle assessments will become commonplace, covering the entire material life cycle from extraction to manufacturing, use, and eventual disposal. This comprehensive assessment will guarantee that F-PSCs are both practical and environmentally responsible. Furthermore, materials for usable substrates will become more critical. To further lessen their impact on the environment, F-PSCs will be made to adhere to substrates made of recycled plastic or bio-based materials. This transition to environmentally friendly substrates is a big step toward improving PSCs' overall sustainability.

A crucial part will also be played by the incorporation of renewable energy sources into manufacturing procedures. Thanks to solar-powered factories and production facilities, F-PSC manufacturing will have a smaller carbon footprint. To further contribute to a cleaner, more sustainable energy landscape, researchers may also investigate the integration of carbon capture and utilization technologies. In the future, sustainable F-PSCs will be subject to international standards and certifications, giving customers and businesses clear guidelines for selecting environmentally friendly solar products. Additionally, as consumers' awareness of sustainability rises, manufacturers will be compelled to prioritize environmental responsibility when developing F-PSC products, giving sustainable solar technologies a competitive edge in the market.

Additionally significant in promoting sustainability in F-PSCs are advocacy and education. The public must be aware of these technologies' environmental benefits to increase adoption and investment in sustainable solar solutions. In conclusion, novel materials, environmentally friendly manufacturing, and a raised awareness of the environment are all integral to the future of flexible perovskite solar cells, and all work together to create a cleaner and more responsible energy landscape.

Researchers will keep pushing PSCs' flexibility and stability boundaries. Expect PSCs to increase their long-term stability and energy conversion efficiencies, making them more dependable for everyday use. Innovative material engineering and device architecture will make this possible. It will become more apparent that F-PSCs are commercially viable. F-PSCs will become a competitive option in the solar energy market as manufacturing costs are expected to be significantly reduced, production methods are improved, and economies of scale are realized. In addition to conventional solar panels, F-PSCs will be used in various other applications. The adaptability of F-PSCs will enable their seamless integration into our daily lives, making renewable energy more available and practical. Examples include solar-powered clothing and accessories and building-integrated PVs.

The flexibility and long-term operational reliability of F-PSCs present challenges for their practical application. When repeatedly deformed, the intrinsic fragility of the perovskite structure can lead to defects and fractures within the perovskite films. In order to make F-PSCs appropriate for general use, it is necessary to incorporate self-healing properties and improve their long-term robustness, which will allow these devices to continue operating for prolonged periods of time. Various tactics have been employed to enhance the mechanical robustness and stability of F-PSCs. These include crystallization control, interface tweaks, self-healing technology integration, component optimization, and grain boundary modifications. Self-healing mechanisms that are triggered by external stimuli are integrated into F-PSCs, enabling them to maintain their stability and function even after they have undergone deformation.

Increasing the mechanical and environmental robustness of F-PSCs is another important aspect of their development and large-scale production. Advanced encapsulation techniques and a variety of barrier materials have been used to lessen the negative effects of moisture and oxygen.

These include thin films, polymer barriers, and polymer matrices infused with nanoparticles. In carefully controlled laboratory settings, these state-of-the-art encapsulation techniques demonstrate significant stability; however, additional investigation is necessary to fully understand their behavior when exposed to oxygen and moisture. Furthermore, cutting-edge encapsulation technologies are still in the early phases of development. Thus, in order to improve the long-term operational reliability of F-PSCs, it is imperative to take into account elements like surface texture, perovskite film composition, crystallinity, additive engineering, and interface modifications. In the future, it is recommended to combine these factors with efficient encapsulation techniques to improve the mechanical and environmental stability of F-PSCs as a whole.

The subject of research will be integrating F-PSCs into smart grids and energy storage systems. This will make it possible to manage intermittent renewable energy sources better, ensuring a steady and reliable power supply even during bad weather. A top priority will continue to be creating sustainable and environmentally friendly materials for F-PSCs. Researchers will keep looking into recyclable and non-toxic components to lessen the environmental impact of the entire production and disposal process. F-PSCs will become more widely used in areas with poor access to traditional energy infrastructure, filling the energy gap in isolated and underdeveloped areas. Their portability and light weight will make it easier to deploy them in disaster-stricken and off-grid areas. It will become more common for materials scientists, engineers, and experts in renewable energy to work together. The advancement of F-PSC technology will be accelerated by interdisciplinary research that results in novel materials, manufacturing techniques, and system integration breakthroughs.

Governments and regulatory agencies will be crucial in determining how F-PSCs develop in the future. Adopting these cutting-edge solar solutions will be accelerated by supportive

policies, incentives, and regulations encouraging investment in research and development. The focus will be on improving the robustness and longevity of F-PSCs to withstand challenging environmental conditions and continue functioning over an extended period. Their appeal for long-term investments will increase as a result. Education and awareness campaigns will help people and businesses understand F-PSCs' advantages, installation options, and maintenance needs as they become more common, promoting a greater acceptance of this clean energy technology.

In conclusion, the development of F-PSCs is up and coming. These solar cells will develop further with ongoing research and development, providing a flexible, affordable, and sustainable solution to our expanding energy needs while lowering our carbon footprint. It is not a question of if, but when, they will be integrated into the conventional energy grid, and they will significantly impact the current state of renewable energy.

#### **ACKNOWLEDGEMENTS:**

This work was supported by the National Research Foundation of Korea (NRF) grant funded by the Korean government (MSIT) (No. RS-2022–00165798). Authors acknowledge support and funding of King Khalid University through Research Center for Advanced Materials Science (RCAMS) under grant no: RCAMS/KKU/001-23.

#### **REFERENCES**

- [1] S. Aftab, M.Z. Iqbal, S. Hussain, F. Kabir, A.A. Al-Kahtani, H.H. Hegazy, *Advanced Functional Materials*, (2023) 2303449.
- [2] J. Tang, H. Liu, D. Zhitomirsky, S. Hoogland, X. Wang, M. Furukawa, L. Levina, E.H. Sargent, *Nano letters*, 12 (2012) 4889-4894.
- [3] S. Aftab, M.Z. Iqbal, S. Hussain, H.H. Hegazy, M.A. Saeed, *Nano Energy*, (2023) 108249.
- [4] N.H. Hemasiri, M. Ashraf, S. Kazim, R. Graf, R. Berger, N. Ullah, M.N. Tahir, S. Ahmad, *Nano Energy*, 109 (2023) 108326.
- [5] S. Aftab, A. Abbas, M.Z. Iqbal, S. Hussain, F. Kabir, H.H. Hegazy, F. Xu, J.H. Kim, B.S. Goud, *Materials Today Energy*, 36 (2023) 101366.
- [6] S. Aftab, M.Z. Iqbal, S. Hussain, H.H. Hegazy, M.A. Saeed, *Nano Energy*, 108 (2023) 108249.

- [7] L. Yang, J. Feng, Z. Liu, Y. Duan, S. Zhan, S. Yang, K. He, Y. Li, Y. Zhou, N. Yuan, *Advanced Materials*, 34 (2022) 2201681.
- [8] T.D. Siegler, A. Dawson, P. Lobaccaro, D. Ung, M.E. Beck, G. Nilsen, L.L. Tinker, *ACS Energy Letters*, 7 (2022) 1728-1734.
- [9] S.W. Lee, S. Bae, D. Kim, H.S. Lee, *Advanced Materials*, 32 (2020) 2002202.
- [10] S. Gu, R. Lin, Q. Han, Y. Gao, H. Tan, J. Zhu, *Advanced Materials*, 32 (2020) 1907392.
- [11] T. Zhu, L. Shen, S. Xun, J.S. Sarmiento, Y. Yang, L. Zheng, H. Li, H. Wang, J.L. Bredas, X. Gong, *Advanced Materials*, 34 (2022) 2109348.
- [12] W. Yang, S.-H. Jo, Y. Tang, J. Park, S.G. Ji, S.H. Cho, Y. Hong, D.-H. Kim, J. Park, E. Yoon, H. Zhou, S.-J. Woo, H. Kim, H.J. Yun, Y.S. Lee, J.Y. Kim, B. Hu, T.-W. Lee, *Advanced Materials*, n/a 2304533.
- [13] C.C. Zhang, Z.K. Wang, S. Yuan, R. Wang, M. Li, M.F. Jimoh, L.S. Liao, Y. Yang, *Advanced Materials*, 31 (2019) 1902222.
- [14] Y. Lin, B. Chen, F. Zhao, X. Zheng, Y. Deng, Y. Shao, Y. Fang, Y. Bai, C. Wang, J. Huang, *Advanced materials*, 29 (2017) 1700607.
- [15] X. Li, S. Aftab, A. Abbas, S. Hussain, M. Aslam, F. Kabir, H.S.M. Abd-Rabboh, H.H. Hegazy, F. Xu, M.Z. Ansari, *Nano Energy*, 118 (2023) 108979.
- [16] H. Chen, Q. Wei, M.I. Saidaminov, F. Wang, A. Johnston, Y. Hou, Z. Peng, K. Xu, W. Zhou, Z. Liu, *Advanced Materials*, 31 (2019) 1903559.
- [17] T. Ibn-Mohammed, S.C.L. Koh, I.M. Reaney, A. Acquaye, G. Schileo, K.B. Mustapha, R. Greenough, *Renewable and Sustainable Energy Reviews*, 80 (2017) 1321-1344.
- [18] J. Chung, S.S. Shin, K. Hwang, G. Kim, K.W. Kim, D.S. Lee, W. Kim, B.S. Ma, Y.-K. Kim, T.-S. Kim, J. Seo, *Energy & Environmental Science*, 13 (2020) 4854-4861.
- [19] M.J. Paik, J.W. Yoo, J. Park, E. Noh, H. Kim, S.-G. Ji, Y.Y. Kim, S.I. Seok, *ACS Energy Letters*, 7 (2022) 1864-1870.
- [20] W. Wang, G. Yu, S. Attique, *Solar RRL*, 7 (2023) 2201064.
- [21] Z. Chen, Q. Cheng, H. Chen, Y. Wu, J. Ding, X. Wu, H. Yang, H. Liu, W. Chen, X. Tang, *Advanced Materials*, (2023) 2300513.
- [22] Z. Yi, X. Li, B. Xiao, Q. Jiang, Y. Luo, J. Yang, *Chemical Engineering Journal*, (2023) 143790.
- [23] P. Docampo, J.M. Ball, M. Darwich, G.E. Eperon, H.J. Snaith, *Nature communications*, 4 (2013) 2761.
- [24] C. Roldán-Carmona, O. Malinkiewicz, A. Soriano, G.M. Espallargas, A. Garcia, P. Reinecke, T. Kroyer, M.I. Dar, M.K. Nazeeruddin, H.J. Bolink, *Energy & Environmental Science*, 7 (2014) 994-997.
- [25] M. Lee, Y. Jo, D.S. Kim, Y. Jun, *Journal of Materials Chemistry A*, 3 (2015) 4129-4133.
- [26] X. Wang, Z. Li, W. Xu, S.A. Kulkarni, S.K. Batabyal, S. Zhang, A. Cao, L.H. Wong, *Nano Energy*, 11 (2015) 728-735.
- [27] M. Lee, Y. Jo, D.S. Kim, H.Y. Jeong, Y. Jun, *Journal of Materials Chemistry A*, 3 (2015) 14592-14597.
- [28] M. Dianetti, F. Di Giacomo, G. Polino, C. Ciceroni, A. Liscio, A. D'Epifanio, S. Licoccia, T. Brown, A. Di Carlo, F. Brunetti, *Solar Energy Materials and Solar Cells*, 140 (2015) 150-157.
- [29] M.M. Tavakoli, K.-H. Tsui, Q. Zhang, J. He, Y. Yao, D. Li, Z. Fan, *ACS nano*, 9 (2015) 10287-10295.
- [30] K.K. Sears, M. Fievez, M. Gao, H.C. Weerasinghe, C.D. Easton, D. Vak, *Solar RRL*, 1 (2017) 1700059.
- [31] I. Jeon, T. Chiba, C. Delacou, Y. Guo, A. Kaskela, O. Reynaud, E.I. Kauppinen, S. Maruyama, Y. Matsuo, *Nano letters*, 15 (2015) 6665-6671.
- [32] Z. Liu, P. You, C. Xie, G. Tang, F. Yan, *Nano Energy*, 28 (2016) 151-157.
- [33] P.L. Qin, Q. He, C. Chen, X.L. Zheng, G. Yang, H. Tao, L.B. Xiong, L. Xiong, G. Li, G.J. Fang, *Solar RRL*, 1 (2017) 1700058.
- [34] C. Bi, B. Chen, H. Wei, S. DeLuca, J. Huang, *Advanced Materials*, 29 (2017) 1605900.
- [35] B. Dou, E.M. Miller, J.A. Christians, E.M. Sanehira, T.R. Klein, F.S. Barnes, S.E. Shaheen, S.M. Garner, S. Ghosh, A. Mallick, *The journal of physical chemistry letters*, 8 (2017) 4960-4966.

- [36] J.H. Heo, D.H. Shin, M.H. Jang, M.L. Lee, M.G. Kang, S.H. Im, *Journal of Materials Chemistry A*, 5 (2017) 21146-21152.
- [37] E. Lee, J. Ahn, H.C. Kwon, S. Ma, K. Kim, S. Yun, J. Moon, *Advanced Energy Materials*, 8 (2018) 1702182.
- [38] J. Yoon, H. Sung, G. Lee, W. Cho, N. Ahn, H.S. Jung, M. Choi, *Energy & Environmental Science*, 10 (2017) 337-345.
- [39] S. Castro-Hermosa, J. Dagar, A. Marsella, T.M. Brown, *IEEE Electron Device Letters*, 38 (2017) 1278-1281.
- [40] J.-I. Park, J.H. Heo, S.-H. Park, K.I. Hong, H.G. Jeong, S.H. Im, H.-K. Kim, *Journal of Power Sources*, 341 (2017) 340-347.
- [41] X.-L. Ou, J. Feng, M. Xu, H.-B. Sun, *Optics Letters*, 42 (2017) 1958-1961.
- [42] M. Xu, J. Feng, Z.-J. Fan, X.-L. Ou, Z.-Y. Zhang, H.-Y. Wang, H.-B. Sun, *Solar Energy Materials and Solar Cells*, 169 (2017) 8-12.
- [43] M. Kaltenbrunner, G. Adam, E.D. Głowacki, M. Drack, R. Schwödiauer, L. Leonat, D.H. Apaydin, H. Groiss, M.C. Scharber, M.S. White, *Nature materials*, 14 (2015) 1032-1039.
- [44] J. Feng, X. Zhu, Z. Yang, X. Zhang, J. Niu, Z. Wang, S. Zuo, S. Priya, S. Liu, D. Yang, *Advanced materials*, 30 (2018) 1801418.
- [45] W. Chen, Y. Wu, J. Fan, A.B. Djurišić, F. Liu, H.W. Tam, A. Ng, C. Surya, W.K. Chan, D. Wang, *Advanced Energy Materials*, 8 (2018) 1703519.
- [46] D. Yang, R. Yang, K. Wang, C. Wu, X. Zhu, J. Feng, X. Ren, G. Fang, S. Priya, S. Liu, *Nature communications*, 9 (2018) 3239.
- [47] G.S. Han, S. Lee, M.L. Duff, F. Qin, J.-K. Lee, *ACS applied materials & interfaces*, 10 (2018) 4697-4704.
- [48] J.H. Heo, D.H. Shin, M.L. Lee, M.G. Kang, S.H. Im, *ACS applied materials & interfaces*, 10 (2018) 31413-31421.
- [49] T. Bu, J. Li, F. Zheng, W. Chen, X. Wen, Z. Ku, Y. Peng, J. Zhong, Y.-B. Cheng, F. Huang, *Nature communications*, 9 (2018) 4609.
- [50] C. Liu, L. Zhang, X. Zhou, J. Gao, W. Chen, X. Wang, B. Xu, *Advanced Functional Materials*, 29 (2019) 1807604.
- [51] M. Zhong, Y. Liang, J. Zhang, Z. Wei, Q. Li, D. Xu, *Journal of Materials Chemistry A*, 7 (2019) 6659-6664.
- [52] M. Li, Y.G. Yang, Z.K. Wang, T. Kang, Q. Wang, S.H. Turren-Cruz, X.Y. Gao, C.S. Hsu, L.S. Liao, A. Abate, *Advanced Materials*, 31 (2019) 1901519.
- [53] G. Lee, M.-c. Kim, Y.W. Choi, N. Ahn, J. Jang, J. Yoon, S.M. Kim, J.-G. Lee, D. Kang, H.S. Jung, *Energy & Environmental Science*, 12 (2019) 3182-3191.
- [54] C. Wu, D. Wang, Y. Zhang, F. Gu, G. Liu, N. Zhu, W. Luo, D. Han, X. Guo, B. Qu, *Advanced Functional Materials*, 29 (2019) 1902974.
- [55] H. Li, X. Li, W. Wang, J. Huang, J. Li, Y. Lu, J. Chang, J. Fang, W. Song, *Solar RRL*, 3 (2019) 1800317.
- [56] K. Zhu, Z. Lu, S. Cong, G. Cheng, P. Ma, Y. Lou, J. Ding, N. Yuan, M.H. Rummeli, G. Zou, *Small*, 15 (2019) 1902878.
- [57] C. Li, S. Cong, Z. Tian, Y. Song, L. Yu, C. Lu, Y. Shao, J. Li, G. Zou, M.H. Rummeli, *Nano Energy*, 60 (2019) 247-256.
- [58] J.E. Kim, S.S. Kim, C. Zuo, M. Gao, D. Vak, D.Y. Kim, *Advanced Functional Materials*, 29 (2019) 1809194.
- [59] M. Li, W.W. Zuo, A.G. Ricciardulli, Y.G. Yang, Y.H. Liu, Q. Wang, K.L. Wang, G.X. Li, M. Saliba, D. Di Girolamo, *Advanced materials*, 32 (2020) 2003422.
- [60] X. Dai, Y. Deng, C.H. Van Brackle, S. Chen, P.N. Rudd, X. Xiao, Y. Lin, B. Chen, J. Huang, *Advanced Energy Materials*, 10 (2020) 1903108.
- [61] X. Meng, Z. Cai, Y. Zhang, X. Hu, Z. Xing, Z. Huang, Z. Huang, Y. Cui, T. Hu, M. Su, *Nature Communications*, 11 (2020) 3016.



- [62] Y.Y. Kim, T.-Y. Yang, R. Suhonen, A. Kemppainen, K. Hwang, N.J. Jeon, J. Seo, *Nature communications*, 11 (2020) 5146.
- [63] V. Babu, R. Fuentes Pineda, T. Ahmad, A.O. Alvarez, L.A. Castriotta, A. Di Carlo, F. Fabregat-Santiago, K. Wojciechowski, *ACS Applied Energy Materials*, 3 (2020) 5126-5134.
- [64] X. Xu, H. Wang, J. Wang, M. Muhammad, Z. Wang, P. Chen, W. Zhao, B. Kang, J. Zhang, C. Li, *ACS Applied Energy Materials*, 3 (2020) 4208-4216.
- [65] W. Deng, F. Li, J. Li, M. Wang, Y. Hu, M. Liu, *Nano Energy*, 70 (2020) 104505.
- [66] G. Jeong, D. Koo, J. Seo, S. Jung, Y. Choi, J. Lee, H. Park, *Nano Letters*, 20 (2020) 3718-3727.
- [67] X. Meng, Z. Xing, X. Hu, Z. Huang, T. Hu, L. Tan, F. Li, Y. Chen, *Angewandte Chemie International Edition*, 59 (2020) 16602-16608.
- [68] X. Hu, X. Meng, X. Yang, Z. Huang, Z. Xing, P. Li, L. Tan, M. Su, F. Li, Y. Chen, *Science Bulletin*, 66 (2021) 527-535.
- [69] L. Yang, Q. Xiong, Y. Li, P. Gao, B. Xu, H. Lin, X. Li, T. Miyasaka, *Journal of Materials Chemistry A*, 9 (2021) 1574-1582.
- [70] Z. Huang, J. Long, R. Dai, X. Hu, L. Le, X. Meng, L. Tan, Y. Chen, *Chemical Communications*, 57 (2021) 6320-6323.
- [71] J. Jin, J. Li, Q. Tai, Y. Chen, D.D. Mishra, W. Deng, J. Xin, S. Guo, B. Xiao, X. Wang, *Journal of Power Sources*, 482 (2021) 228953.
- [72] D.H. Jung, Y.J. Oh, Y.S. Nam, H. Lee, *Journal of Alloys and Compounds*, 850 (2021) 156752.
- [73] Z. Wu, P. Li, J. Zhao, T. Xiao, H. Hu, P. Sun, Z. Wu, J. Hao, C. Sun, H. Zhang, *Advanced Materials Interfaces*, 8 (2021) 2001512.
- [74] X. Yu, Z. Li, X. Sun, C. Zhong, Z. Zhu, A.K.-Y. Jen, *Nano Energy*, 82 (2021) 105701.
- [75] E. Cho, Y.Y. Kim, D.S. Ham, J.H. Lee, J.-S. Park, J. Seo, S.-J. Lee, *Nano Energy*, 82 (2021) 105737.
- [76] Z. Li, X. Wu, S. Wu, D. Gao, H. Dong, F. Huang, X. Hu, A.K.-Y. Jen, Z. Zhu, *Nano Energy*, 93 (2022) 106853.
- [77] Z. Dai, S. Li, X. Liu, M. Chen, C.E. Athanasiou, B.W. Sheldon, H. Gao, P. Guo, N.P. Padture, *Advanced Materials*, 34 (2022) 2205301.
- [78] B. Fan, J. Xiong, Y. Zhang, C. Gong, F. Li, X. Meng, X. Hu, Z. Yuan, F. Wang, Y. Chen, *Advanced Materials*, 34 (2022) 2201840.
- [79] Y. Yan, R. Wang, Q. Dong, Y. Yin, L. Zhang, Z. Su, C. Wang, J. Feng, M. Wang, J. Liu, *Energy & Environmental Science*, 15 (2022) 5168-5180.
- [80] J. Kurisinkal Pious, Y. Zwirner, H. Lai, S. Olthof, Q. Jeangros, E. Gilshtein, R.K. Kothandaraman, K. Artuk, P. Wechsler, C. Chen, *ACS Applied Materials & Interfaces*, 15 (2023) 10150-10157.
- [81] J. Dou, Q. Song, Y. Ma, H. Wang, G. Yuan, X. Wei, X. Niu, S. Ma, X. Yang, J. Dou, *Journal of Energy Chemistry*, 76 (2023) 288-294.
- [82] S. Li, Y. Li, Y. Li, F. Deng, X. Sun, X. Tao, *Solar Energy Materials and Solar Cells*, 257 (2023) 112391.
- [83] L. Zhang, C. Fu, S. Wang, M. Wang, R. Wang, S. Xiang, Z. Wang, J. Liu, H. Ma, Y. Wang, *Advanced Functional Materials*, 33 (2023) 2213961.
- [84] Z. Skafi, J. Xu, V. Mottaghitalab, L. Mivehi, B. Taheri, F. Jafarzadeh, S.K. Podapangi, D. Altamura, M.R. Guascito, L. Barba, C. Giannini, A. Rizzo, F. De Rossi, H. Javanbakht Lomeri, L. Sorbello, F. Matteocci, F. Brunetti, T.M. Brown, *Solar RRL*, n/a 2300324.
- [85] L. Li, Y. Wang, X. Wang, R. Lin, X. Luo, Z. Liu, K. Zhou, S. Xiong, Q. Bao, G. Chen, *Nature Energy*, 7 (2022) 708-717.
- [86] L. Li, Y. Wang, X. Wang, R. Lin, X. Luo, Z. Liu, K. Zhou, S. Xiong, Q. Bao, G. Chen, Y. Tian, Y. Deng, K. Xiao, J. Wu, M.I. Saidaminov, H. Lin, C.-Q. Ma, Z. Zhao, Y. Wu, L. Zhang, H. Tan, *Nature Energy*, 7 (2022) 708-717.
- [87] D. Glowienka, Y. Galagan, *Advanced Materials*, 34 (2022) 2105920.

- [88] N. Yang, C. Zhu, Y. Chen, H. Zai, C. Wang, X. Wang, H. Wang, S. Ma, Z. Gao, X. Wang, *Energy & Environmental Science*, 13 (2020) 4344-4352.
- [89] Y. Zhan, F. Yang, W. Chen, H. Chen, Y. Shen, Y. Li, Y. Li, *Advanced Materials*, 33 (2021) 2105170.
- [90] P. Liu, Y. Xian, W. Yuan, Y. Long, K. Liu, N.U. Rahman, W. Li, J. Fan, *Advanced Energy Materials*, 10 (2020) 1903654.
- [91] J. Wu, S. Liu, Z. Li, S. Wang, D. Xue, Y. Lin, J. Hu, 2021.
- [92] F. Qiao, D. Du, W. Shen, W. Wang, Z. Chen, C. Gao, L. He, Z. Lü, H. Liu, *Solar RRL*.
- [93] Z. Xie, W. Xu, S. Sun, X. Xie, Y. Li, G. Qin, *Journal of Materials Chemistry A*, 8 (2020) 12821-12832.
- [94] Q. Jiang, J. Tong, Y. Xian, R.A. Kerner, S.P. Dunfield, C. Xiao, R.A. Scheidt, D. Kuciauskas, X. Wang, M.P. Hautzinger, *Nature*, 611 (2022) 278-283.
- [95] Z. Li, B. Li, X. Wu, S.A. Sheppard, S. Zhang, D. Gao, N.J. Long, Z. Zhu, *Science*, 376 (2022) 416-420.
- [96] S. Liu, V.P. Biju, Y. Qi, W. Chen, Z. Liu, *NPG Asia Materials*, 15 (2023) 27.
- [97] Z. Dai, S.K. Yadavalli, M. Chen, A. Abbaspourtamijani, Y. Qi, N.P. Padture, *Science*, 372 (2021) 618-622.
- [98] Q. Dong, M. Chen, Y. Liu, F.T. Eickemeyer, W. Zhao, Z. Dai, Y. Yin, C. Jiang, J. Feng, S. Jin, *Joule*, 5 (2021) 1587-1601.
- [99] J. Shi, H. Zhang, X. Xu, D. Li, Y. Luo, Q. Meng, *Small*, 12 (2016) 5288-5294.
- [100] Y. Wu, G. Xu, J. Xi, Y. Shen, X. Wu, X. Tang, J. Ding, H. Yang, Q. Cheng, Z. Chen, *Joule*, 7 (2023) 398-415.
- [101] O.Y. Gong, G.S. Han, S. Lee, M.K. Seo, C. Sohn, G.W. Yoon, J. Jang, J.M. Lee, J.H. Choi, D.-K. Lee, *ACS Energy Letters*, 7 (2022) 2893-2903.
- [102] D. Gao, B. Li, Z. Li, X. Wu, S. Zhang, D. Zhao, X. Jiang, C. Zhang, Y. Wang, Z. Li, *Advanced Materials*, 35 (2023) 2206387.
- [103] M. Li, J. Zhou, L. Tan, H. Li, Y. Liu, C. Jiang, Y. Ye, L. Ding, W. Tress, C. Yi, *The Innovation*, 3 (2022).

#### CRediT authorship contribution statement

**Sikandar Aftab**: Supervision, Conceptualization, Methodology, software, Writing- Original draft preparation, Writing- Reviewing and Editing the manuscript: **Sajjad Hussain**: Proofread the Original draft and Editing the manuscript: **Fahmid Kabir, Muhammad Aslam, Altaf Hussain Rajpar, and Abdullah G. Al-Sehemi** : Facilitate to design a comparison table and Figures

#### Declaration of Competing Interest

The authors declare no competing interests.

## Highlights

1. Flexible perovskite solar cells (PSCs) combine high efficiency with adaptability, making them a hot topic in clean energy research.
2. This review explores cutting-edge strategies to enhance PSC flexibility, stability, and cost-effectiveness.
3. Key developments include flexible all-perovskite tandem solar cells, reducing perovskite grain boundary impact, dual-interface reinforcement, 2D and 3D material fusion, and eco-friendly carbon-based materials.
4. These advancements have the potential to revolutionize renewable energy and accelerate the integration of adaptable solar solutions into the energy grid.
5. This analysis provides insights into the exciting trends driving flexible PSC innovation in clean energy.